CAPITAL UNIVERSITY OF SCIENCE AND TECHNOLOGY, ISLAMABAD

Numerical Investigation on the Effects of Geometrical Parameters on the Performance of a Steam Ejector

by

Muhammad Ahsan Waqar Khan

A thesis submitted in partial fulfillment for the degree of Master of Science

in the

Faculty of Engineering
Department of Mechanical Engineering

2025

To My Family, Teachers & Fellows

CERTIFICATE OF APPROVAL

Numerical Investigation on the Effects of Geometrical Parameters on the Performance of a Steam Ejector

by

Muhammad Ahsan Waqar Khan

(MME211001)

THESIS EXAMINING COMMITTEE

S. No.	Examiner	Name	Organization
(a)	External Examiner	Dr. Talha Irfan Khan	IST, Islamabad
(b)	Internal Examiner	Dr. M. Mahabat Khan	CUST, Islamabad
(c)	Supervisor	Dr. Muhammad Irfan	CUST, Islamabad

Dr. Muhammad Irfan
Thesis Supervisor
January, 2025

Dr. M. Mahabat Khan
Head
Dept. of Mechanical Engineering
January, 2025

Dr. Imtiaz Ahmad Taj
Dean
Faculty of Engineering
January, 2025

Author's Declaration

I, **Muhammad Ahsan Waqar Khan** hereby state that my MS thesis titled "**Numerical Investigation on the Effects of Geometrical Parameters on the Performance of a Steam Ejector**" is my own work and has not been submitted previously by me for taking any degree from Capital University of Science and Technology, Islamabad or anywhere else in the country/abroad.

At any time if my statement is found to be incorrect even after my graduation, the University has the right to withdraw my MS Degree.

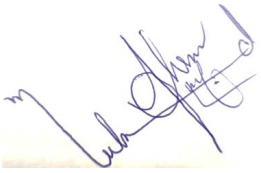

(Muhammad Ahsan Waqar Khan)

Registration No: MME211001

Plagiarism Undertaking

I solemnly declare that the research work presented in this thesis titled "**Numerical Investigation on the Effects of Geometrical Parameters on the Performance of a Steam Ejector**" is solely my research work with no significant contribution from any other person. Small contribution/help wherever taken has been duly acknowledged and that complete thesis has been written by me.

I understand the zero tolerance policy of the HEC and Capital University of Science and Technology towards plagiarism. Therefore, I as an author of the above titled thesis declare that no portion of my thesis has been plagiarized and any material used as reference is properly referred/cited.

I undertake that if I am found guilty of any formal plagiarism in the above titled thesis even after award of MS Degree, the University reserves the right to withdraw/revoke my MS degree and that HEC and the University have the right to publish my name on the HEC/University website on which names of students are placed who submitted plagiarized work.

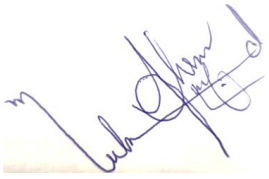

(Muhammad Ahsan Waqar Khan)

Registration No: MME211001

Acknowledgement

I extend my heartfelt gratitude to the **Almighty Allah** for His bountiful blessings and for endowing me with the strength and perseverance to complete this thesis report. My profound respect is dedicated to **His Holy Prophet (PBUH)**, whose teachings illuminate the path of knowledge and guidance for all of humanity.

I am deeply grateful to my esteemed supervisor, Engr. Dr. Muhammad Irfan, for affording me the invaluable opportunity to probe into this field and for his diligent supervision, insightful discussions, and expert guidance, especially during the challenging periods of my health crises. I extend my heartfelt thanks to Mr. Dr. M. Mahabat Khan (HOD) for his constant encouragement and ingenious insights, which have been pivotal in shaping the success of this work. I am also thankful to Dr. M. Faheem Siddiqui for his invaluable support through out the research phase. Additionally, I acknowledge with gratitude the boundless support moral, financial, and emotional from my beloved family, valued friends, and well-wishers, who stood by me persistently throughout this fulfilling journey.

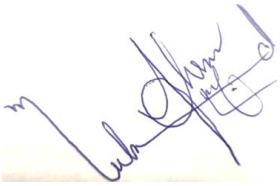

(Muhammad Ahsan Waqar Khan)

Abstract

The operational and geometrical parameters greatly impact performance metrics of an ejector. The current research employs numerical methods to analyze how geometric parameters influence a steam ejector performance when applied in refrigeration system. The standard ejector studied by Dong et al. using steam as the working fluid is investigated in this research. The study considers two lengths of the mixing chamber: l_m = 20 mm and 60 mm. The primary nozzle position (NXP) is systematically changed in mixing chamber as it is moved towards the constant area section (CAS). This study is carried out for four different values of Mach numbers: Ma = 2, 3, 4 and 5. These Mach numbers are achieved by varying exit diameters of nozzle. A commercial computational tool ANSYS Fluent is used to perform the simulations. The performance parameters under investigation are the entrainment ratio (ω) and the critical back pressure (P_{cr}). Numerical solution procedure is validated by comparing the present results against the literature. It is observed that Ma = 2, 3 and 4 are the cases of under-expansion with decreasing level of intensity in the order, whereas, Ma = 5 is the case of over-expansion. The shock train generated by the primary fluid jet decides the available area for entrainment of vapor coming from evaporator (secondary vapor) and eventually dictates ω. The P_{cr} increases as momentum of fluid increases; however, an increased velocity of the jet may result in stronger secondary shock in the diffuser of ejector thereby decreasing P_{cr}. It is observed that both the performance metrics, i.e., ω and P_{cr} become independent of the Mach number existing at the exit plane of the primary convergent-divergent nozzle when its exit is at the inlet plane or inside the unifor area section. For l_m = 20 mm, performance parameters are maximum at NXP = -10 mm corresponding to a primary nozzle distance of 30 mm from the inlet of the constant area section. Similarly, for l_m = 60 mm, the maximum values of performance parameters are reported at NXP = 20 mm which corresponds to the primary nozzle distance of 40 mm from the inlet of the constant area section. This suggests that the steam ejector performs best when the primary nozzle exit is placed at a distance of 30 – 40 mm from the inlet plane of the CAS, irrespective of the primary nozzle Ma number.

Contents

Author's Declaration iv

Plagiarism Undertaking v

Acknowledgement vi

Abstract vii

List of Figures x

List of Tables xii

Abbreviations xiii

Symbols xiv

1 Introduction 1

1.1 Motivation . . . 1
1.2 Ejector Refrigeration System . . . 2
1.3 Ejector – The key Component . . . 2
1.4 Ejector Models Based on Primary Nozzle Position . . . 4
1.4.1 Constant Pressure Mixing . . . 4
1.4.2 Constant Area Mixing . . . 5
1.5 Performance Indicators of an Ejector . . . 6
1.5.1 Entrainment Ratio (ω) . . . 6
1.5.2 Coefficient of Performance (COP) . . . 6
1.5.3 Pressure Lift Ratio (PLR) . . . 7
1.5.4 Critical Back Pressure (P_{cr}) . . . 7
1.6 The Modes of Ejector Operation . . . 7
1.6.1 Critical Mode . . . 7
1.6.2 Sub-critical Mode . . . 8
1.6.3 Back Flow Mode . . . 8
1.7 Working Fluid – Refrigerant . . . 8
1.7.1 Chemical and Environmental Stability . . . 9
1.7.2 High Latent Heat of Vaporization . . . 9
1.7.3 Specific Heat Properties . . . 9

1.7.4 Moderate Pressure at Boiler Temperature . . . 9
1.7.5 Favorable Thermal and Viscous Transport Properties . . . 10
1.7.6 Compressibility Factor Close to Unity . . . 10
1.7.7 High Molecular Weight . . . 10
1.8 Flow Structures in Ejector . . . 10
1.9 Objectives . . . 11
1.10 Thesis Layout . . . 12

2 Literature Review **14**
2.1 Development of Ejector Technology . . . 14
2.2 Key Contributions in Literature . . . 14
2.3 Research Gap and Current Research Objectives . . . 21

3 Problem Formulation and Numerical Solution Methodology **24**
3.1 Geometric Configuration . . . 24
3.1.1 Ma At Primary Nozzle Exit . . . 24
3.1.2 Mixing Chamber Length (l_m) . . . 25
3.1.3 Primary Nozzle Position (NXP) . . . 26
3.2 Mathematical Formulation . . . 26
3.3 Flow Solver . . . 27
3.3.1 Turbulence Modeling . . . 27
3.3.2 Boundary Conditions . . . 29
3.3.3 Grid Independence . . . 29
3.4 Validation of Numerical Solution Procedure . . . 30

4 Results and Discussion **33**
4.1 Variation of Entrainment Ratio with NXP . . . 34
4.1.1 $\boldsymbol{l_m}$ = 20 mm . . . 34
4.1.2 $\boldsymbol{l_m}$ = 60 mm . . . 44
4.2 Variation of Critical Back Pressure with NXP . . . 49
4.2.1 $\boldsymbol{l_m}$ = 20 mm . . . 50
4.2.2 $\boldsymbol{l_m}$ = 60 mm . . . 52
4.3 Comparative Plots of Performance Parameters for $\boldsymbol{l_m}$ = 20 mm and $\boldsymbol{l_m}$ = 60 mm . . . 53

5 Conclusion and Future Recommendations **57**
5.1 Future Recommendations . . . 59

Bibliography **60**

List of Figures

1.1 Schematic of an ejector refrigeration system . . . 3
1.2 The schematic diagram of an ejector along with the velocity and pressure profiles at the centerline during the operation. . . . 4
1.3 Constant pressure mode of ejector operation . . . 5
1.4 Constant Area Model of Ejector Operation . . . 6
1.5 Modes of the ejector operation . . . 8
1.6 Shock waves structures generated in CAS of an ejector [6] . . . 11

3.1 A Schematic diagram of an ejector mentioning the important geometrical nomenclature . . . 25
3.2 Mesh convergence results showing the Ma plots at centerline of an ejector using three mesh resolutions . . . 30
3.3 Validation study – (a) ω and (b) p_{cr} of the present numerical study compared with the results of Dong et al. [7] for various mixing chamber lengths . . . 31

4.1 Schematic diagram of the object ejector geometry. The fixed geometric dimensions (in mm) are mentioned numerically on the figure. The variable geometric parameters are mentioned using the symbols-details are mentioned in Table 4.1 . . . 34
4.2 The line plots of Ma number plotted against the length of the ejector along the centreline for all the Ma number cases. The plots are generated for NXP = 0 for all the cases. . . . 34
4.3 Line plots of the entrainment ratio for all the Ma number cases plotted against the exit position of the primary nozzle (NXP) for (a) $l_m = 20\,\text{mm}$ and (b) $l_m = 60\,\text{mm}$ . . . 35
4.4 The contour plots of Mach number for Ma = 2 case for $l_m = 20\,\text{mm}$ and varying NXP values . . . 36
4.5 The contour plots of pressure gradient for Ma = 2 case for $l_m = 20\,\text{mm}$ and varying NXP values . . . 38
4.6 The contour plots of density gradient for Ma = 2 case for $l_m = 20\,\text{mm}$ and varying NXP values . . . 39
4.7 The contour plots of density gradient for Ma = 2 case for $l_m = 20\,\text{mm}$ and varying NXP values . . . 40
4.8 The contour plots of Mach number for Ma = 3 case for $l_m = 20\,\text{mm}$ and varying NXP values . . . 41
4.9 The contour plots of Mach number for Ma = 4 case for $l_m = 20\,\text{mm}$ and varying NXP values . . . 42

4.10 The contour plots of Mach number for Ma = 5 case for $l_m = 20\,\text{mm}$ and varying NXP values 43
4.11 The contour plots of Mach number for Ma = 2 case for $l_m = 60\,\text{mm}$ and varying NXP values 45
4.12 The contour plots of Mach number for Ma = 3 case for $l_m = 60\,\text{mm}$ and varying NXP values 47
4.13 The contour plots of Mach number for Ma = 4 case for $l_m = 60\,\text{mm}$ and varying NXP values 48
4.14 The contour plots of Mach number for Ma = 5 case for $l_m = 60\,\text{mm}$ and varying NXP values 49
4.15 The contours of Ma number plotted for varying values of condenser pressure 50
4.16 Line plots of the P_{cr} for all Ma number cases plotted against the NXP for (a) $l_m = 20\,\text{mm}$ and (b) $l_m = 60\,\text{mm}$ 52
4.17 The performance parameters (a) Entrainment ratio and (b) Critical back pressure plotted for Ma = 2 for $l_m = 20\,\text{mm}$ and $l_m = 60\,\text{mm}$ for different values of NXP. 54
4.18 The performance parameters (a) Entrainment ratio and (b) Critical back pressure plotted for Ma = 3 for $l_m = 20\,\text{mm}$ and $l_m = 60\,\text{mm}$ for different values of NXP. 54
4.19 The performance parameters (a) Entrainment ratio and (b) Critical back pressure plotted for Ma = 4 for $l_m = 20\,\text{mm}$ and $l_m = 60\,\text{mm}$ for different values of NXP. 55
4.20 The performance parameters (a) ω and (b) P_{cr} plotted for Ma = 5.0 for $l_m = 20\,\text{mm}$ and $l_m = 60\,\text{mm}$ for different values of NXP. . . 56

List of Tables

3.1 The geometric parameters and the corresponding numerical values of the ejector considered for the investigation [7] 25
3.2 The NXP values considered for two values of mixing chamber length 26
3.3 Mesh convergence data showing the % difference in the values of the entrainment ratio 31

4.1 Geometric variables and their numerical values investigated in this study 33

Abbreviations

ANN	Artificial neural network
CAS	Constant Area Section
COP	Coefficient of performance
CD	Convergent divergent
CFD	Computational fluid dynamics
DoE	Design of Experiment
NXP	Primary nozzle position
SP	Movable spindle
SIMPLEC	Semi-Implicit Method for Pressure-Linked Equations Consistent
VGE	Variable geometry ejector

Symbols

$2D$	Two dimensional
$3D$	Three dimensional
d_i	Primary nozzle inlet diameter
d_n	Primary nozzle throat diameter
θ_1	Primary nozzle diffuser divergent angle
d_a	Primary nozzle exit diameter
d_m	Secondary nozzle inlet diameter
d_c	Constant area section diameter
Δh_e	Enthalpy changes in evaporator
Δh_g	Enthalpy changes in generator
k	Specific heat ratio
l_m	Mixing chamber length
l_c	Constant area section length
l_d	Diffuser length
$\dot{m}_s$	Secondary flow rate
$\dot{m}_p$	Primary flow rate
Ma	Mach number
P_{cr}	Critical back pressure
P_c	Condenser pressure
θ_2	Secondary nozzle diffuser divergent angle
ω	Entrainment ratio

Chapter 1

Introduction

1.1 Motivation

The demand for energy-efficient and environmentally sustainable cooling technologies is increasing day by day, particularly in light of the significant energy consumption associated with conventional vapor compression systems. Currently, vapor compression refrigeration and air conditioning systems contribute to roughly 20% of global electricity consumption [1]. This poses a significant demand for energy resources and results in the generation of high greenhouse gas emissions. The reliance on energy-intensive compressors, which require electricity to maintain cooling, highlights the need for alternative technologies that can achieve similar cooling performance with reduced environmental impact.

An alternative solution lies in the use of ejector-based refrigeration systems, which eliminate the need for compressors and instead rely on ejectors powered by solar energy or waste heat. Ejectors utilize low-grade heat to drive the refrigeration cycle, offering a low-cost alternative that is particularly suited to regions with ample solar resources or industries with waste heat available. This approach reduces the electricity demand and enables the utilization of renewable or otherwise underutilized heat sources, aligning with sustainable energy objectives.

Implementing ejector-driven refrigeration systems presents multiple benefits. By reducing reliance on high-quality electrical energy, these systems can lessen peak

loads on electric utility providers, contributing to grid stability and resilience. Furthermore, with reduced electrical input, ejector-based systems can significantly lower greenhouse gas emissions compared to conventional methods, contributing to climate change mitigation efforts. These advantages underscore the potential of ejector-based cooling systems to transform the refrigeration and air conditioning sectors by providing an energy-efficient, environmentally friendly alternative to vapor compression systems.

1.2 Ejector Refrigeration System

The process flow diagram representing the operation of ejector operated refrigeration system indicating the key components, is shown in Figure 1.1. In this system, a generator or boiler produces high-pressure and high-temperature refrigerant vapor by utilizing waste heat or solar energy. This vapor, referred to as the primary vapor, serves as the driving force for the system. The primary vapor (denoted as state 1) enters the ejector, where it undergoes expansion in the primary converging-diverging nozzle, accelerating to supersonic velocities. This expansion creates a zone of low-pressure in the mixing chamber of the ejector, resulting a pressure gradient between an evaporator and the ejector. This pressure gradient drives the flow of secondary refrigerant vapor into the ejector (state 2), which comes from the evaporator of the refrigerator. Inside the ejector, both the secondary and the primary vapor streams mix, and the resulting mixture is compressed through a series of shock waves. The compressed vapor stream exits the ejector (state 3) and enters the condenser, where it undergoes the condensation phase change into a liquid state. The liquid refrigerant coming out of the condenser (state 4) is subdivided into two parts. One part flows back to generator (state 5) after being pumped through a liquid recirculation pump, while the other stream passes through an expansion device and enters the evaporator (state 6). Inside the evaporator, the working fluid/refrigerant absorbs heat from its surroundings, causing it to evaporate and produce the desired cooling effect.

1.3 Ejector – The key Component

The ejector serves as the core device in the ejector operated refrigeration system, playing critical function to determine system's overall performance. Its design

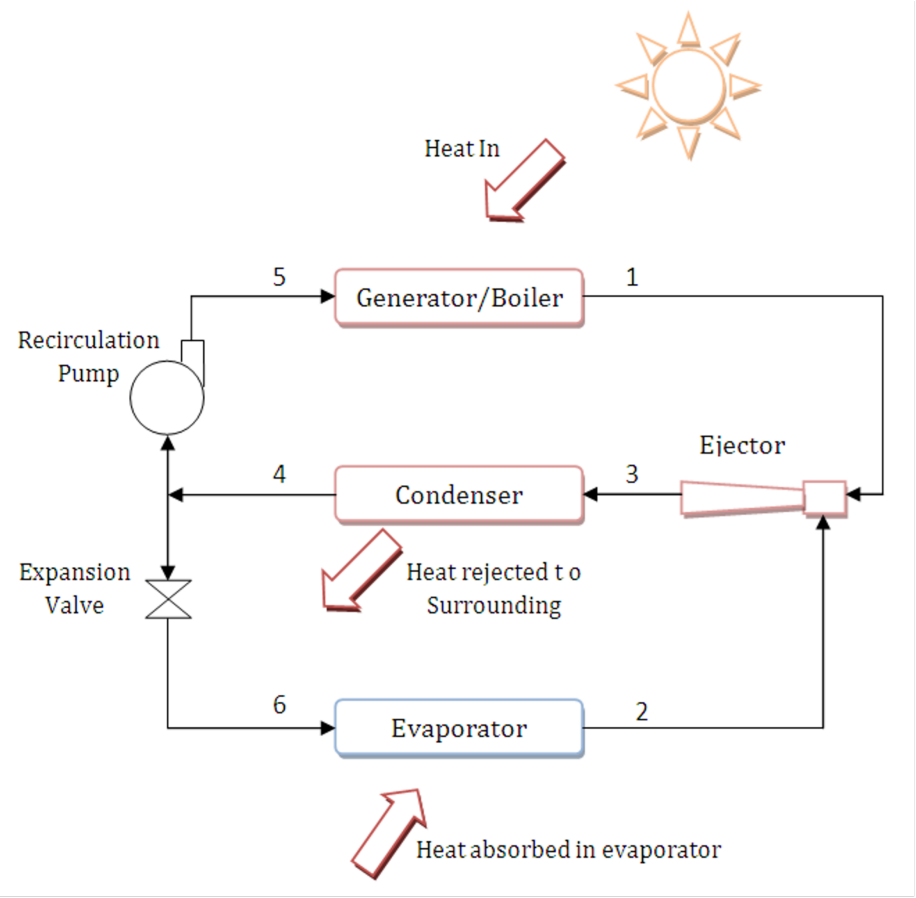

FIGURE 1.1: Schematic of an ejector refrigeration system

and operation significantly influence the efficiency of the entire refrigeration cycle. Figure 1.2 presents a schematic of the ejector along with its pressure and velocity profiles, illustrating the operational principles [2]. A high-pressure primary vapor produced by generator enters the ejector at inlet point '1' Within the primary converging-diverging nozzle, this vapor undergoes expansion, accelerating to supersonic velocities. This process generates low-pressure pockets at the exit region of the primary nozzle, facilitating the flow of secondary vapor stream from the evaporator at point '2.' The pressure differential between the evaporator and the ejector drives this secondary flow.

The primary vapor emerging from the nozzle fans out, creating a converging passage that induces the acceleration of the vapor stream coming from the secondary source (evaporator) to sonic velocity. This critical velocity occurs at a hypothetical area referred to as the "effective area," representing a virtual throat where the two streams interact dynamically. Beyond this point, the primary and secondary vapor streams begin to mix. The mixed stream continues through the ejector,

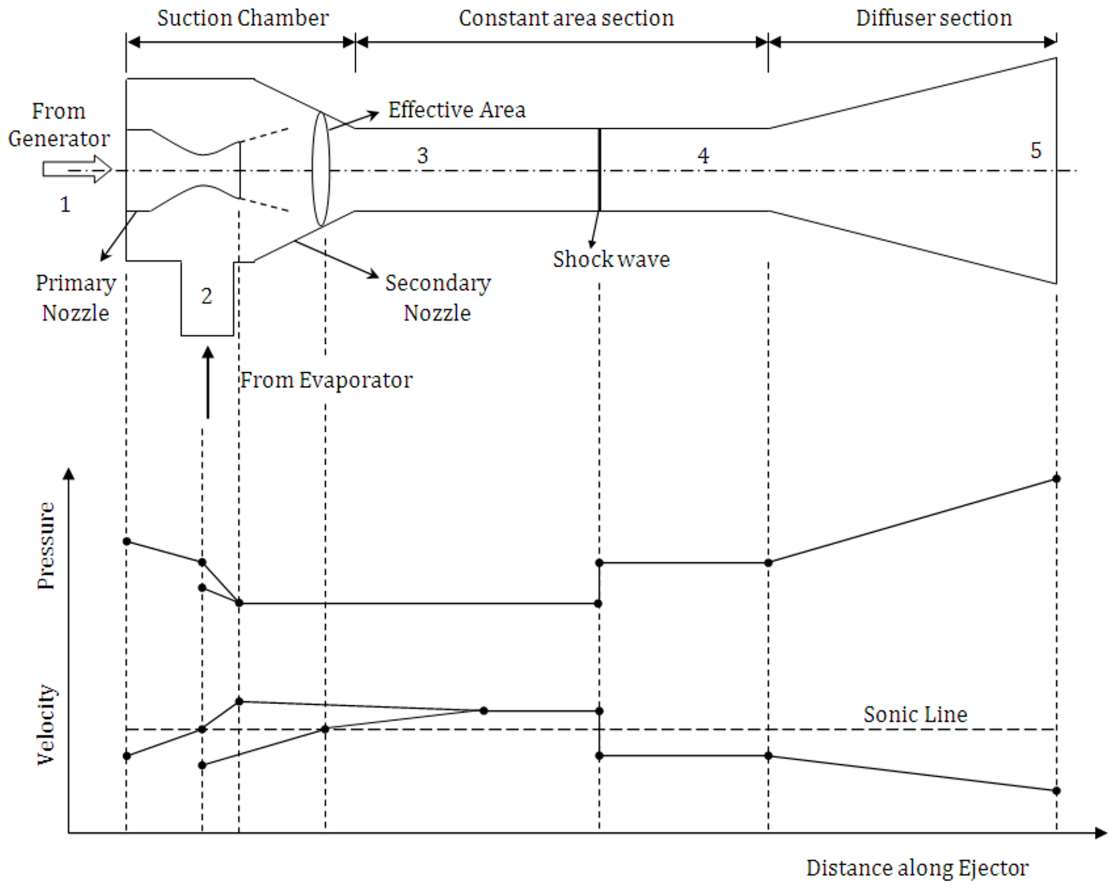

FIGURE 1.2: The schematic diagram of an ejector along with the velocity and pressure profiles at the centerline during the operation.

where complete mixing occurs in section '3' called the "constant area section". A shock wave is generated in this section based on the upstream flow conditions. This shock wave facilitates compression by increasing the pressure of the mixed stream and transitioning it to subsonic flow conditions at point '4.' The subsonic mixed stream undergoes further compression in the diffuser section before exiting the ejector at point '5' and entering the condenser. This intricate process ensures effective energy transfer and contributes to the desired performance of the refrigeration system [2].

1.4 Ejector Models Based on Primary Nozzle Position

1.4.1 Constant Pressure Mixing

This model has been widely adopted by researchers investigating ejector refrigeration systems [3]. This model serves as a benchmark for understanding and

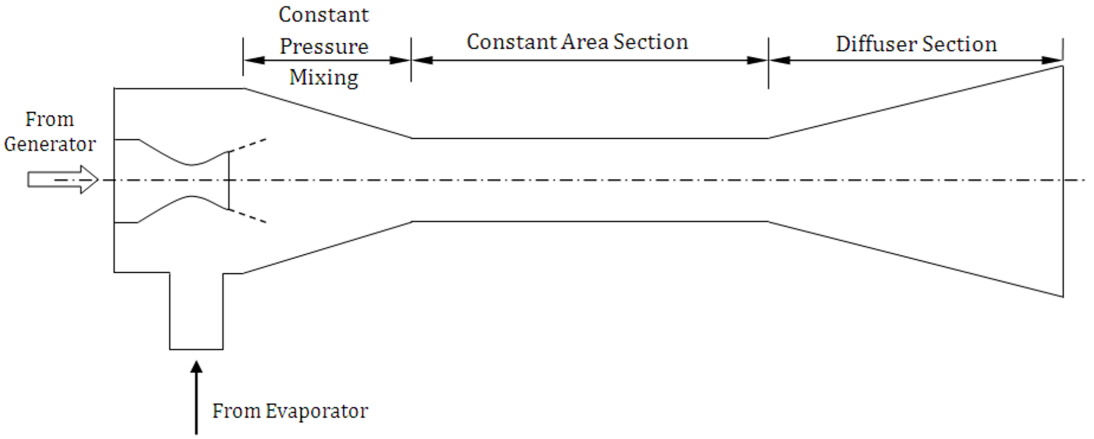

FIGURE 1.3: Constant pressure mode of ejector operation

analyzing the flow dynamics within ejectors. According to this model, the mixing of the primary vapor stream coming from the generator and the secondary vapor stream coming from the evaporator takes place at a constant pressure, as illustrated in Figure 1.3.

A shock wave may develop in the CAS to compress working fluid. After the constant area section (CAS), diffuser section then further compresses the subsonic fluid, resulting in an additional pressure rise. The key assumptions employed for this model are as follows.

1. Stagnation properties at the entry and the outlet of the ejector
2. Uniform flow velocities at all the sections of the ejector
3. Constant pressure mixing of the fluid streams
4. The shock wave creates subsonic flow in the CAS

The mathematical models governing the flow of fluid in the ejector include the continuity, momentum and energy equations. Additionally, the refrigerant may be treated as an ideal gas.

1.4.2 Constant Area Mixing

In this case, primary jet exits in the CAS. Therefore, primary and secondary streams of working fluid will mix in the CAS. Apart from mixing method and

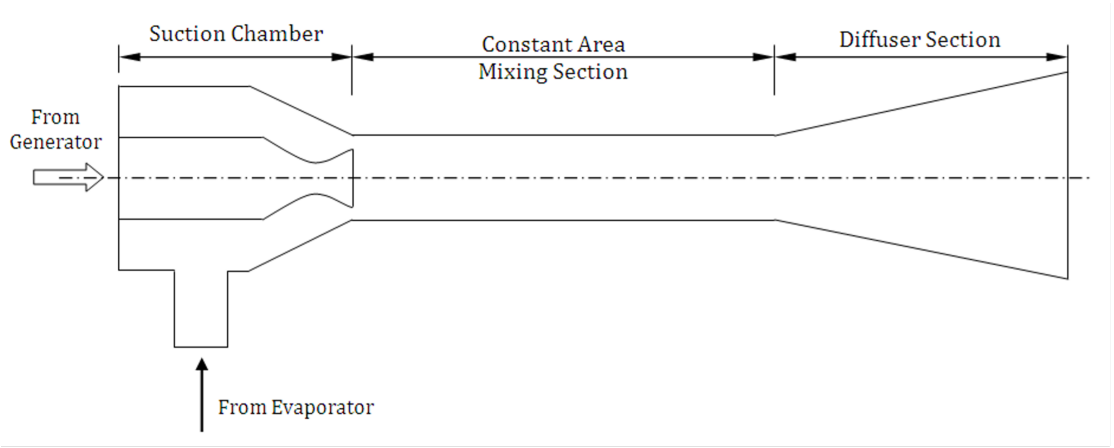

FIGURE 1.4: Constant Area Model of Ejector Operation

the specific region where mixing occurs, the assumptions used for analyzing the flow within this ejector are consistent with those of the one-dimensional constant-pressure ejector flow model. Figure 1.4 schematically shows the constant area mixing ejector.

1.5 Performance Indicators of an Ejector

The efficiency and effectiveness of an ejector are evaluated based on the following performance metrics.

1.5.1 Entrainment Ratio (ω)

It is the ratio of the mass flow rate of refrigerant coming from the evaporator (secondary flow) and the mass flow rate of refrigerant moving through primary nozzle. The mathematical expression for ω is

$$\omega = \frac{\dot{m}_s}{\dot{m}_p} \tag{1.1}$$

Where $\dot{m}_s$ stands for mass flow rate of the refrigerant vapor coming from the secondary source, i.e., evaporator while $\dot{m}_p$ indicates the primary refrigerant mass flow rate coming directly from the generator.

1.5.2 Coefficient of Performance (COP)

It is defined as

$$COP = \frac{\dot{m}_s \Delta h_e}{\dot{m}_p \Delta h_g + W_{mec}} \tag{1.2}$$

Where, Δh_g and Δh_e are the enthalpy changes in the generator and evaporator, respectively, while W_{mec} is the mechanical energy required by the pump and can be neglected. Incorporating the definition of the entrainment ratio into the Equation (1.2) yields the mathematical form of COP as follows

$$COP = \omega \frac{\Delta h_e}{\Delta h_g} \tag{1.3}$$

Therefore, COP is dependent on ω of the system.

1.5.3 Pressure Lift Ratio (PLR)

It is a measure of the degree of compression attained through the operation of an ejector. It is defined as ratio of static pressure at the diffuser exit to the static pressure in the evaporator.

1.5.4 Critical Back Pressure (P_{cr})

It is the maximum value of condenser pressure after which the ω starts decreasing. This corresponds to a decrease in the working capacity of the system. An ejector having a large value of the P_{cr} will make sure a smooth working of the system over a wider range of operational conditions without any fluctuation in the system performance.

1.6 The Modes of Ejector Operation

There are three modes of operation of the ejector based on the condenser pressure of the system. These three modes are schematically presented in Figure 1.5.

1.6.1 Critical Mode

If the condenser pressure P_c is less than the P_{cr}, then the ejector will operate at its maximum design entrainment ratio. This mode is also called the double choking mode because both streams will flow at its maximum capacity, i.e., both the streams are choked. Operating the ejector in critical mode is preferred because it ensures the most stable and reliable performance.

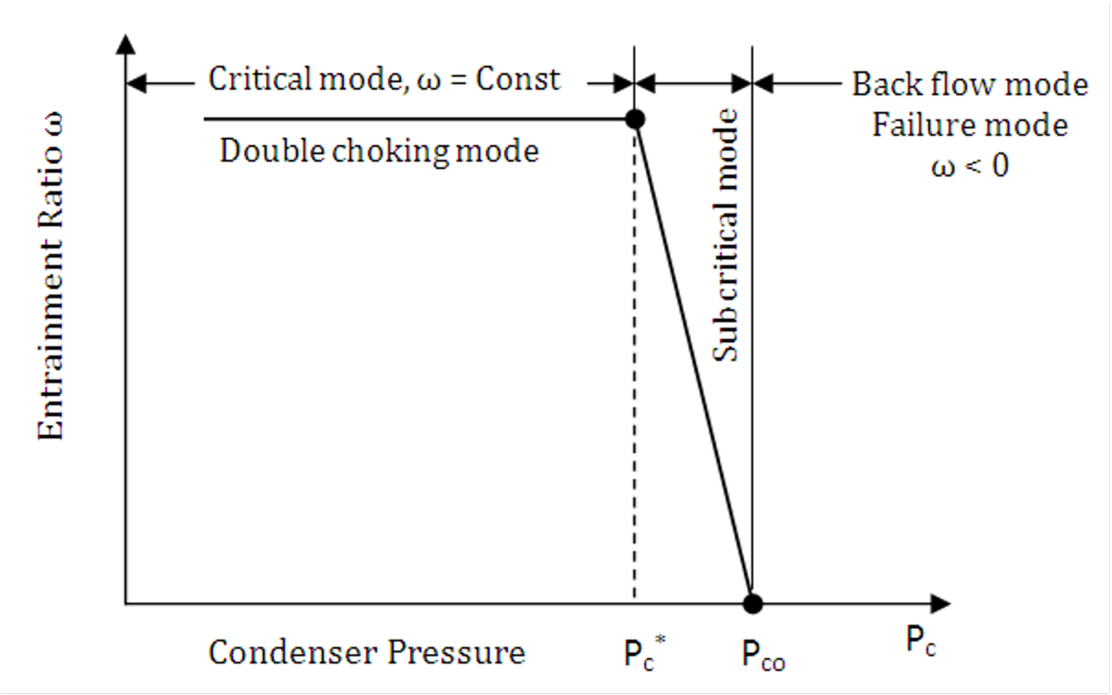

FIGURE 1.5: Modes of the ejector operation

1.6.2 Sub-critical Mode

An ejector is said to be operating in the sub-critical or the single choking mode if $P_{cr} < P_c < P_{co}$ as illustrated in Figure 1.5. In this mode of operation, the compression wave or the shock wave travels into mixing chamber, disrupting the mix up of secondary and primary refrigerant streams. Consequently, the choking is not attained for the flow coming from the evaporator side, i.e., the secondary flow. The flow becomes unstable and the secondary flow rate to fluctuates causing the entrainment ratio to decrease significantly.

1.6.3 Back Flow Mode

In this mode of operation, $P_c > P_{co}$ and the functionality of the ejector is totally seized. This mode of ejector operation will lead to the failure of associated refrigeration system.

1.7 Working Fluid – Refrigerant

The choice of refrigerant is an important consideration from the point of view of the performance of an ejector refrigeration system. Selecting an appropriate refrigerant

can significantly enhance system efficiency. Researchers have explored a wide range of refrigerants tailored to specific operating conditions, economic constraints, and environmental considerations. A suitable refrigerant should ideally possess the following characteristics [4], [5]:

1.7.1 Chemical and Environmental Stability

The refrigerant must have chemical stability, readily available, non-flammable, non-corrosive, non-explosive, environmentally safe, and economically viable.

1.7.2 High Latent Heat of Vaporization

It minimizes the required mass flow rate, thereby reducing power requirements and enhancing the COP.

1.7.3 Specific Heat Properties

For optimal system performance, the refrigerant should possess a low specific heat capacity in the liquid phase to facilitate effective subcooling, allowing the refrigerant to store more thermal energy while remaining in the liquid state. Additionally, a high specific heat capacity in the vapor phase is desirable to restrict the extent of the superheating region, thereby ensuring better thermal regulation. These combined characteristics contribute significantly to enhancing the overall efficiency of the system.

1.7.4 Moderate Pressure at Boiler Temperature

At the boiler operating temperature, the fluid's pressure should remain within moderate limits. Excessively high pressures would necessitate the use of robust and heavy-duty pressure vessels, increasing material costs and structural complexity. Additionally, higher pressures would place greater demands on the pump, resulting in increased energy consumption and operational costs.

1.7.5 Favorable Thermal and Viscous Transport Properties

Properties such as viscosity and thermal conductivity should support efficient heat transfer.

1.7.6 Compressibility Factor Close to Unity

A refrigerant with a compressibility factor near 1 simplifies the design process by making the ideal gas assumption more applicable to ejector design.

1.7.7 High Molecular Weight

A higher molecular weight enables the use of smaller ejector components for a given system capacity, simplifying construction and enhancing performance. Experimental observations suggest that increasing molecular weight improves the entrainment ratio, COP, and ejector efficiency.

1.8 Flow Structures in Ejector

Ejector refrigeration systems represent an innovative approach to cooling, employing thermal energy instead of a traditional mechanical compressor to drive the refrigeration cycle. This unique design makes use of an ejector, which compresses refrigerant vapors through a series of shock waves generated within the ejector itself. The thermally driven nature of this system, along with the inherent simplicity of the ejector mechanism, makes it highly attractive for applications in the refrigeration and air conditioning industry. Additionally, the absence of a mechanical compressor offers an environmentally friendly alternative, as it reduces reliance on electricity and lowers greenhouse gas emissions, aligning well with sustainable energy goals. Performance of an ejector refrigeration device, however, is not straightforward and is influenced by a complex interplay of operational and geometric parameters. Parameters such as the ejector's geometry, the nature of the working fluid, and operational conditions (such as pressure and temperature) have significant impacts on system performance. These parameters do not only

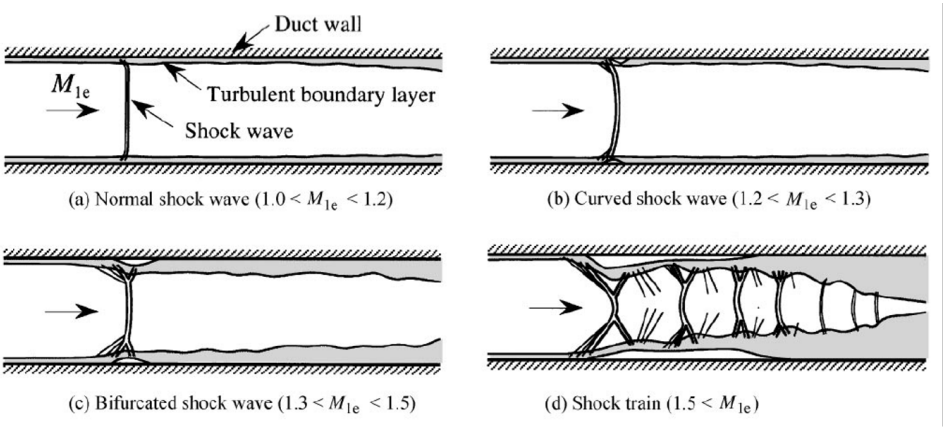

FIGURE 1.6: Shock waves structures generated in CAS of an ejector [6]

affect overall efficiency but also interact in complex ways within the ejector. A unique aspect of the ejector mechanism is the creation of a series of shock waves as the fluid moves through it. These shock waves are crucial for the compression process, as the shock-shock and shock-ejector body interactions directly influence the refrigerant's flow dynamics and overall energy transfer in the system. The Figure 1.6 presents a variety of shock wave structures generated within the the CAS of the ejector and their complex interactions for various ranges of Mach numbers [6].

A notable challenge in optimizing ejector refrigeration systems lies in the variability of system behavior across different working fluids and geometric configurations. Each fluid interacts uniquely with the shock structures within the ejector, requiring careful selection and analysis to achieve optimal system performance. As a result, researchers are actively investigating the impacts of various operating and geometric parameters to develop a clearer understanding of ejector dynamics. The goal of the current research is to establish general conclusions regarding the behavior of ejector refrigeration systems under different configurations and conditions, which would facilitate their widespread application and improve their efficiency for industrial and commercial uses.

1.9 Objectives

This thesis presents a numerical study conducted using ANSYS Fluent to explore the effects of two key geometric features of ejector on its performance metrics

for a standard steam ejector designed by Dong et al. [7] for refrigeration applications. Specifically, it focuses on the position of the primary nozzle inside the secondary nozzle, i.e., NXP and the mixing chamber length (l_m), examining how this positioning affects system performance. In this study, two different lengths of the mixing chamber are considered to assess their influence on performance. The main performance metrics evaluated are the P_{cr} and the ω. The performance parameter ω serves as an indicator of the COP of the system, offering insight into its efficiency. All other operational and geometric conditions are maintained as specified in the reference study by Dong et al. [7], allowing for a focused analysis of the selected parameters.

1.10 Thesis Layout

The thesis layout is as follows:

Chapter 1 outlines the motivation and objectives of the research. It also provides a concise overview of the ejector refrigeration system, including its key characteristics, flow structures inside the ejector and performance metrics.

Chapter 2 reviews the relevant literature, establishing the foundation for this study and positioning it as a novel contribution to the field. This chapter discusses prior research on ejector refrigeration systems, highlighting the research gaps that this thesis aims to address.

Chapter 3 outlines the problem formulation, presenting the geometrical details of the system under study. It describes the numerical solution procedure employed in this research, including grid convergence and validation studies.

Chapter 4 presents a comprehensive analysis of the results, focusing effects of selected geometrical variables on the efficiency and output of an ejector refrigeration

system. This discussion examines flow structures within the ejector and interprets the implications of these results with respect to efficiency and overall performance.

Finally, Chapter 5 provides the conclusions of the thesis work, summarizing the key findings and offering insights into potential areas which need more research efforts.

Chapter 2

Literature Review

2.1 Development of Ejector Technology

Sir Charles Parsons first invented the ejector in 1901, with its initial application being in a steam engine condenser. In 1910, Maurice Leblanc introduced the ejector into the field of refrigeration, marking its first use for cooling applications. By the 1930s, ejector-based refrigeration systems had gained recognition and were applied in air-conditioning systems [2]. However, the advent of vapor compression refrigeration systems posed a significant challenge to ejector refrigeration systems. The superior performance and efficiency of vapor compression systems led to their widespread adoption, overshadowing the development of ejector refrigeration technologies. Interest in ejector refrigeration systems was revived following the energy crisis of the 1970s, as energy shortages in certain regions heightened the need for alternative and renewable energy solutions. This period saw a rapid expansion in research and development of renewable energy technologies, particularly solar energy. Concurrently, solar cooling systems, including ejector-based refrigeration systems, became a growing focus for researchers aiming to develop sustainable and energy-efficient cooling technologies.

2.2 Key Contributions in Literature

Extensive literature exists on ejector refrigeration systems, reflecting the growing interest and advancements in this field over time. Several review papers have provided comprehensive summaries of these developments, consolidating knowledge

and highlighting key contributions. Among these, Besagni et al. [8]. presented an extensive review focusing on the use of ejectors in air conditioning and refrigeration systems. Their research provides significant perspectives on the development of ejector-based technologies and highlights their importance in contemporary cooling systems. Tashtoush et al. [9] conducted another notable review that examined ejector design methods, performance characteristics, and applications in refrigeration systems. Their study also emphasized the geometric aspects of ejector design, discussing how advancements in geometry have been utilized to improve system performance.

The efficiency of an ejector in an ejector-based air conditioning and refrigeration system is significantly influenced by both the operational and geometrical parameters. Several authors have explored the effects of operational parameters on the ejector performance. Pianthong et al. [10] conducted numerical simulations to analyze the effects of boiler and evaporator temperatures on the steam ejector refrigeration system using CFD code. Their results highlight optimum operating conditions regarding the design of an ejector for refrigeration applications. Guo et al. [11] performed thorough investigation to analyze the system performance for a range of operating parameters which they declared as the "full operating conditions". They validated their model for a number of refrigerants and got good results. Anan et al. [12] proposed double-stage ejector refrigeration system and presented results for four refrigerants: R600a, R134a, R1234yf and R290. Zeinab Sajjadi et al. [13] proposed a novel designed ejector cooling system and evaluated the effects of variation in the operational parameters on the system performance. Ogaili et al. [14] performed detailed analysis of ejector refrigeration cycle integrated with parabolic trough and organic Rankine cycle. They evaluated the economic performance analysis that is crucial for the widespread utilization of the technology.

The geometrical parameters of the ejector plays a critical role in determining the performance of the ejector refrigeration system. The important geometrical parameters include the position of the primary nozzle in the mixing chamber, the length of the mixing chamber and the primary nozzle throat diameter, the diameter of the constant area section and the diffuser geometry. Additionally, the

choice of working fluid is another vital consideration, as it impacts not only the system's performance but also its environmental sustainability. The selection of an appropriate refrigerant requires careful analysis to balance thermodynamic properties with ecological concerns. The literature includes numerous studies where researchers have explored various geometrical parameters to evaluate their effects on performance metrics such as the entrainment ratio, critical back pressure, and system efficiency. These investigations have provided valuable insights into optimizing ejector designs for enhanced functionality and environmental compliance.

Aphornratana and Eames [15] conducted experiments on an ejector refrigerator using steam as the working fluid with an axially adjustable primary nozzle. The study examined the effects of nozzle position on the coefficient of performance and cooling capacity. Varga et al. performed a numerical study to examine the effects of area ratio, constant area section length and the primary nozzle exit position (NXP) on the performance of a steam ejector. They suggested the integration of a spindle within the primary nozzle as a means to regulate and optimize the primary flow rate. This design modification enables better adaptation to fluctuating operating conditions, ensuring more precise control over the flow dynamics and enhancing the overall efficiency of the system [16]. Ma et al. carried out an experimental investigation focusing on an innovative steam jet refrigeration system specifically engineered for applications utilizing solar energy. The system utilized a spindle to regulate the primary flow within the ejector, enabling precise control and achieving optimal operational performance and coefficient of performance [17].

Ruangtrakoon et al. [18] experimentally investigated a 1 kW steam jet refrigeration system using eight primary nozzles with varying geometries. A total of six nozzles were designed with throat diameters varying from 1.4 mm to 2.6 mm, each nozzle achieving a Mach number of 4.0 at the exit. The other two nozzles, both having a 1.4 mm throat diameter, were distinguished by exit Mach numbers of 3.0 and 5.5, respectively. The results demonstrated that the geometric parameters of the primary nozzle significantly influenced ejector performance and the system's COP. A numerical study was also performed by Ruangtrakoon et al. [19] in which they examined in detail how different primary nozzle geometries influence the performance characteristics of an ejector when used within a jet refrigeration

system utilizing steam as the refrigerant. Mach number contours were analyzed to illustrate the mixing processes within the ejector. The findings of the study highlighted that two key factors significantly affected the performance of the ejector: the location of shock waves within the mixed fluid flow and the expansion angle of the primary fluid jet stream as it traveled through the mixing chamber. These elements were determined to play a crucial role in optimizing the ejector's operational efficiency.

Pereira et al. [20] conducted an experimental study using the first laboratory-scale variable geometry ejector (VGE) with isobutane (R600a) as the refrigerant. The research was designed to have control and vary two important geometric parameters: the ejector area ratio and the exit position of the primary nozzle. The outcomes of the investigation showcased the exceptional performance of the ejector, emphasizing the importance of these parameters in achieving optimal efficiency with the COP values in the range 0.4 - 0.8, based on the operational parameter conditions. Additionally, the advantages of the variable geometry design were compared to those of a fixed geometry ejector. For instance, at a condenser pressure of 3 bar, the variable geometry ejector achieved an 80% improvement in COP compared to the fixed geometry configuration. Chen et al. [21] experimentally confirmed that the nozzle exit position is a critical structural parameter influencing ejector performance. Their study examined the critical entrainment ratios at various nozzle exit positions, revealing that the critical entrainment ratio initially increases with the nozzle exit position before reaching a constant value.

Understanding the crucial role of geometric parameters, Yan et al. [22] carried out an experimental study to assess how three specific geometric parameters influence the performance of an ejector operating with R134A as the working refrigerant. These parameters included the nozzle exit position, the length of the constant-area section, and the diverging angle of the primary nozzle. The research aimed to provide a comprehensive understanding of how these design variables impact ejector efficiency and functionality. The findings indicated that the nozzle exit position had a more pronounced effect on the ejector performance as compared to the other two parameters. Furthermore, the study identified the most effective geometric configurations and associated dimensionless parameters, which were then

compared with those observed in systems functioning at reduced condensation pressures. This investigation offered clear and practical design recommendations for ejectors, making them more applicable and useful in real-world engineering scenarios. Fu et al. [23] also carried out a numerical investigation to examine the impact of the primary nozzle parameters on the performance of steam ejectors. Their analysis focused on the effects of the primary nozzle outlet diameter and length of the divergent section under varying entrained stream pressures. The findings revealed a significant increase in the entrainment ratio as the nozzle outlet diameter is increased up to an optimal value, after which it begins to decline. This indicates the existence of an optimal range for the nozzle outlet diameter that maximizes ejector performance. Additionally, it was observed that the divergent section length has a relatively minor influence on overall ejector performance. Further investigating the role of primary nozzle position in the ejctor performance, Zhang et al. [24] carried out a comprehensive numerical analysis to investigate the variations in the nozzle position and its impact on the key performance metrics of an ejector. Specifically, the study focused on evaluating the pressure lift ratio, entrainment ratio and the overall efficiency of the ejector utilizing R600a as the working fluid. The findings of the study suggested 6 mm as an optimal nozzle position determined under specific operating conditions and a set ejector geometry. This configuration was shown to deliver the highest entrainment ratio and maximize overall ejector performance. Nevertheless, enhancing the entrainment ratio necessitates a greater suction flow mass and a corresponding increase in energy input. As a result, the system's ability to achieve a significant pressure lift remains relatively constrained. Further exploring the critical role of the primary nozzle in the ejector's performance, Thongtip and Aphornratana [25] performed experiments to investigate the influence of the primary nozzle on the ejector performance using R141b as the refrigerant. The study varied the primary CD nozzle area ratio to gauge its impact on the performance metrics of an ejector. A set of six primary nozzles with different throat diameters, area ratios, and exit Mach numbers were tested. The analysis focused on how changes in the primary nozzle throat diameter and exit Mach number affected the momentum of the primary flow and, consequently, the ejector's performance. The findings suggested that a larger nozzle throat, operating at lower boiler/generator temperatures, is more

effective. Additionally, the primary nozzle exit Mach number should be maximized, and the exit diameter must be compatible with the mixing chamber design for optimal performance. Ramesh and Sekhar [26] emphasized the importance of a comprehensive knowledge of the ejector operation in order to understand and improve the performance of ejector-operated refrigeration systems. Their study focused on the critical geometrical factors, including the mixing chamber angle entraining the secondary flow and the primary nozzle position (NXP), in a steam-operated ejector. They performed their investigation using both CFD simulations and experimental techniques. They examined the interaction between operational conditions and these geometrical parameters, identifying optimal values under specific conditions. For an evaporator capacity of 0.7 kW at a cooling temperature of 10 10° C, a mixing chamber angle of 12 degrees and a primary nozzle position of 24.7 mm yielded the best results, corresponding to generator and condenser pressures of 2 bar and 43 mbar, respectively. Yan et al. [27] made significant changes in the working cycle and proposed a novel ejector-based multi-evaporator refrigeration cycle, targeting its application in refrigerated truck systems operating in tropical regions. Through numerical investigations utilizing CFD techniques, they optimized the geometries of the ejector's primary nozzle for both fixed and variable NXP. Key contributions included identifying the optimal primary nozzle throat diameter to meet the cooling demands under specific operating conditions. For a fixed primary nozzle position (NXP), they extensively analyzed the effects of the angle and the length of the converging portion of the primary nozzle on the system performance.

Thongtip and Aphornratana [28] conducted an experimental investigation to explore the impact of varying primary nozzle area ratios on the operational performance of an ejector refrigeration system utilizing R141b as the working fluid. The study focused on three distinct primary nozzles, each designed with the same throat diameter but differing in area ratios, which resulted in variations in their exit Mach numbers. These nozzles were tested in combination with a mixing chamber featuring a throat diameter of 9 mm. The researchers identified two key evaporator temperature thresholds: the lower and upper critical evaporator temperatures. The results demonstrated that changes in the nozzle exit Mach number, along with adjustments in the primary fluid mass flow rate achieved by varying the

generator temperatures, significantly influenced these critical temperature points. These variations, in turn, had a pronounced effect on the overall performance of the ejector system. Focusing the geometry as the key player in the performance, Van Nguyen et al. [29] carried out an experimental study to assess how a variable geometry ejector (VGE) design influences the performance of a solar-powered ejector air-conditioning system with a cooling capacity of 1.5 kW. The research focused on understanding the effects of adjustable ejector geometry on system efficiency, aiming to enhance its suitability for solar-driven cooling applications. The study demonstrated that the VGE outperformed the fixed-geometry ejector in terms of adaptability and efficiency. The variable geometry ejector (VGE) design featured two key adjustable components: a movable spindle (SP) and a nozzle exit position (NXP) that could be altered to adapt to changing operating conditions. The experimental results demonstrated that the cooling cycle operated consistently and reliably across all test scenarios. Both the NXP and SP were shown to have a significant impact on the overall performance of the system. An optimal primary nozzle position was found, which remained unchanged regardless of variations in operating conditions. In contrast, the optimal position of the SP was found to be dependent on specific operating parameters, highlighting its role in fine-tuning system performance for varying scenarios. Galindo et al. [30] also conducted a performance evaluation of two solar-driven jet-ejector refrigeration system architectures using numerical methods. The first system employed a jet ejector with a fixed geometry, where the area ratio remained constant during operation. In contrast, the second system was equipped with an adjustable spindle mechanism that allowed for dynamic modification of the jet ejector's area ratio. The experimental results revealed that the system with the adjustable spindle ejector offered significant advantages. It enabled continuous and stable operation over a wider range of outdoor environmental conditions, demonstrating its superior adaptability compared to the fixed-geometry counterpart. Abbady et al. [31] also highlighted the need to investigate the geometric parameters and stressed that fixed-geometry ejectors are unable to meet the full range of performance requirements under fluctuating operating conditions. They performed numerical simulations to investigate the performance of a Variable Geometry Ejector (VGE) designed with two key adjustable features: a movable spindle and an adjustable

primary nozzle to vary its exit position. The system utilized R1234yf as the working fluid. A comprehensive Design of Experiment (DoE) analysis was conducted to determine the factors that most significantly influenced the mass flow rates of the primary and secondary streams. In addition, an artificial neural network (ANN) model was developed to accurately predict the ejector's entrainment ratio. This model integrated both operating conditions and geometrical parameters, achieving an exceptional level of accuracy with a coefficient of determination (R^2) of 99.81%. Guo et al. carried out a detailed numerical study aimed at optimizing the working of a steam ejector. Their investigation involved analyzing a wide array of geometric parameters, including dimensions and configurations of key ejector components. Additionally, they examined various operating conditions, such as pressure and temperature ranges, to identify the most effective combination of factors [32]. Their study identified the constant cross-sectional diameter as a key parameter significantly influencing the ejector's entrainment capacity.

Fingas et al. [33] developed an adjustable geometry gas ejector by incorporating a spindle and conducted experimental tests using R290 as the working fluid. The research centered on analyzing key performance parameters of the ejector, particularly the mass entrainment ratio and the critical operating temperature. The findings revealed that adjusting the spindle to reduce the effective throat area significantly enhanced the system's efficiency, resulting in an increase in the entrainment ratio by 35%. Moreover, the ability to fine-tune the spindle position allowed for a substantial decrease in the primary nozzle flow, with reductions reaching up to 65%. This adjustment was achieved without compromising the ejector's ability to maintain the suction capacity of the secondary flow, demonstrating the effectiveness of the spindle mechanism in optimizing overall performance.

2.3 Research Gap and Current Research Objectives

A review of the existing literature highlights significant interest in understanding how the geometric parameters influence the performance of ejectors in refrigeration and air conditioning applications. Among these parameters, the position

of the primary nozzle has been identified as a critical factor affecting operational efficiency. To explore and investigate its effect, researchers have incorporated spindle mechanisms to precisely control both the position of the primary nozzle and the flow passing through it. Despite these advancements, there remains a notable gap in research regarding the combined influence of primary nozzle position and varying mixing section lengths, particularly when operating under different nozzle exit Mach numbers. This area of study requires further exploration to gain deeper insights into its impact on ejector performance.

The current research seeks to bridge the existing research gap by conducting a systematic investigation into the performance of a steam ejector, designed by Dong et al. [7]. In their work, Dong et al. [7] performed three-dimensional numerical simulations to investigate the influence of mixing chamber length on the steam ejector performance. They also varied the primary nozzle exit Mach numbers, and the lengths of the diffuser section and constant area section. The study's results demonstrated a distinct trend in the behavior of the entrainment ratio and the critical back pressure as the length of the mixing chamber was varied. Initially, extending the mixing chamber length led to an increase in both the entrainment ratio and the critical back pressure. However, beyond a certain point, further elongation of the mixing chamber caused a decline in these performance metrics. This observation highlights the existence of an optimal mixing chamber length for achieving maximum efficiency and effectiveness in ejector operation. The analysis revealed that the ejector exhibited optimal performance when the length of the mixing chamber was maintained within the range of 40 mm to 80 mm. This performance was achieved under typical operating conditions of a steam ejector refrigeration system, with the nozzle throat diameter specifically set at 2.5 mm. In their work, however, they did not explored the effects of varying the primary nozzle position in the mixing chamber which has been declared as the most critical geometrical parameter affecting the performance of ejector refrigeration system.

The current analysis focuses on exploring the effects of varying the primary nozzle position in combination with different lengths of the mixing chamber for different nozzle exit Mach numbers. The primary objective of this research is to generate valuable data, discussion and inferences that will help to decide on positioning

the primary nozzle in the mixing chamber for enhancing ejector performance. This discussion will eventually contribute towards the optimization of the ejector geometry to enhance the ejector's efficiency and overall performance, particularly under specific operational conditions.

Chapter 3

Problem Formulation and Numerical Solution Methodology

3.1 Geometric Configuration

The geometric parameters of an ejector significantly influence the overall efficiency of an ejector refrigeration system. This research investigates the impact of important geometrical variables on the key performance indicators for a steam ejector initially designed by Dong et al. While the previous studies explored the effects of l_m on the performance of a steam ejector across various Ma numbers, the current investigation extends this work by examining the influence of the primary nozzle position (NXP). This analysis is conducted for two distinct mixing chamber lengths, considering a primary nozzle exit Ma in the 2 - 5. A schematic of an ejector highlighting the geometric parameters is shown in Figure 3.1. The working fluid used in the ejector is steam. The details of the geometric dimensions are given in Table 3.1. In the geometric configuration shown, the NXP is said to be zero, when primary nozzle exit is situated at the entrance of the converging section of the secondary nozzle of the ejector. Three main geometric features investigated in this study are explained below:

3.1.1 Ma At Primary Nozzle Exit

This is an important parameter that will govern the suction pressure generated in the mixing chamber. This suction effect will act as a driving force to draw

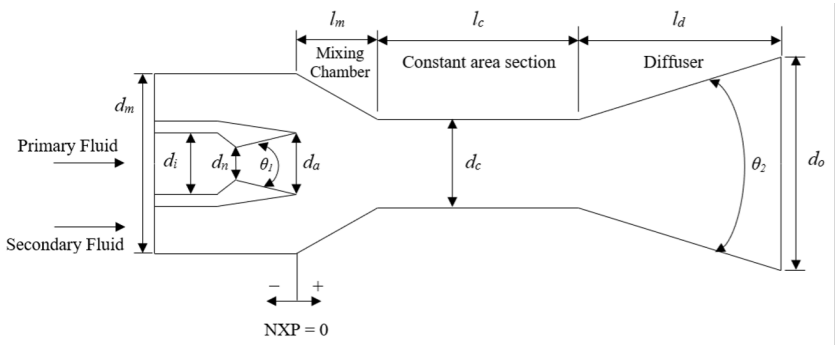

FIGURE 3.1: A Schematic diagram of an ejector mentioning the important geometrical nomenclature

TABLE 3.1: The geometric parameters and the corresponding numerical values of the ejector considered for the investigation [7]

Parameter	**Value**
d_i	10 mm
d_n	2.5 mm
θ_1	10°
d_a	3.3 mm (Ma = 2), 5.6 mm (Ma = 3), 10.4 mm (Ma = 4), 16.4 mm (Ma = 5)
d_m	80 mm
d_c	25 mm
l_m	20, 60 mm
l_c	55 mm
l_d	200 mm
θ_2	16°

secondary vapor from evaporator. This will eventually dictate the ω of the ejector. The Ma at the exit of the primary nozzle is guided by the exit diameter (d_a) of the said convergent divergent nozzle.The mathematical relationship between these two parameters is given by the following isentropic expression.

$$\left(\frac{d_a}{d_n}\right)^2 = \sqrt{\frac{1}{M_a^2}\left[\frac{2+(k-1)M_a^2}{(k+1)}\right]^{\frac{k+1}{k-1}}} \tag{3.1}$$

In present study, four Ma values are used: 2, 3, 4 and 5. The corresponding values of the d_a are 3.3 mm, 5.6 mm, 10 mm and 16.4 mm, respectively.

3.1.2 Mixing Chamber Length (l_m)

The mixing chamber is another crucial geometric feature that provides the space for the mix up of the primary fluid stream and the entrained fluid stream. This will

eventually affect the momentum of the flow and the efficiency of the ejector in an ejector refrigeration system. Two values of l_m are used in the current investigation: 20 mm and 60 mm.

3.1.3 Primary Nozzle Position (NXP)

This is another critical geometric parameter that governs the ejector's output. The variation of the primary nozzle position is also linked to the l_m. In the present study the NXP values used corresponding to the two value of l_m are listed in the Table 3.2.

TABLE 3.2: The NXP values considered for two values of mixing chamber length

l_m (mm)	**NXP** (mm)
20	-15, -10, -5, 0, 5, 10, 15, 20, 25
60	-30, -20, -10, 0, 10, 20, 30, 40, 50, 60, 70

The NXP investigation is performed for all the Ma numbers considered in this study. The remaining geometrical parameters are the same as mentioned in Table 3.1.

3.2 Mathematical Formulation

The governing equations to model the fluid flow in an ejector include continuity, momentum and energy equations. These are expressed as

$$\frac{\partial \rho}{\partial t} + \frac{\partial}{\partial x_i}\left(\rho u_i\right) = 0 \tag{3.2}$$

$$\frac{\partial}{\partial t}\left(\rho u_i\right) + \frac{\partial}{\partial x_i}\left(\rho u_i u_j\right) = -\frac{\partial P}{\partial x_i} + \frac{\partial \tau_{ij}}{\partial x_j} \tag{3.3}$$

$$\frac{\partial}{\partial t}\left(\rho E\right) + \frac{\partial}{\partial x_i}\left[u_i\left(\rho E + P\right)\right] = \vec{\nabla}.\left(\alpha_{eff}\frac{\partial T}{\partial x_i}\right) + \vec{\nabla}.\left[u_j(\tau_{ij})\right] \tag{3.4}$$

$$\rho = \frac{P}{RT} \tag{3.5}$$

$$\text{with } \tau_{ij} = \mu_{eff}\left(\frac{\partial u_i}{\partial x_j} + \frac{\partial u_j}{\partial x_i}\right) - \frac{2}{3}\mu_{eff}\frac{\partial u_k}{\partial x_k}\delta_{ij} \tag{3.6}$$

3.3 Flow Solver

The flow within an ejector is generally characterized as compressible and turbulent. To numerically solve the mathematical model outlined in the relevant section, the commercial CFD solver ANSYS Fluent is used. To simplify solution procedure, a set of assumptions are adopted as follows:

1. The steam at the inlet of the primary nozzle is dry and saturated
2. The steam from the evaporator entering the secondary nozzle is also dry and saturated
3. The steam is considered as an ideal gas
4. The ejector walls are assumed as adiabatic
5. There is steady-state flow in the ejector.

The ejector is modeled as 2D axisymmetric geometry to manage the computational load while producing results representative of 3D geometry Pianthong et al. [10]. A pressure-based solver is used to solve the nonlinear model equations. Steam is considered as the working fluid treating it as an ideal gas. The thermophysical properties of the steam are taken from the default NIST database available in Fluent. The SIMPLEC (Semi-Implicit Method for Pressure-Linked Equations Consistent) algorithm is utilized to solve the flow field within the ejector. This algorithm is particularly effective in addressing pressure-velocity coupling in computational fluid dynamics simulations, ensuring accurate and efficient convergence of the solution. A second-order upwind scheme is employed to discretize the convective terms in the governing equations. This approach enhances accuracy of computational solution by considering flow direction and interpolating variable values from upstream nodes. The second-order upwind scheme effectively minimizes numerical diffusion, ensuring a more precise representation of the flow field.

3.3.1 Turbulence Modeling

The choice of an appropriate turbulence model for a specific problem is influenced by the problem's characteristics, conditions, and context. This decision-making

process becomes particularly challenging in ejector analyses due to the intricate flow patterns within the ejector and the significant sensitivity of its performance to both operating and geometric parameters.

Turbulence modeling remains an active area of research, attracting significant attention from the scientific community. Numerous experimental and computational studies have been conducted, yielding conflicting conclusions. While some researchers advocate for the application of the $k-\omega$ turbulence model Bartosiewicz et al. [34], the majority favor the $k-\epsilon$ turbulence model for such analyses. The Realizable $k-\epsilon$ turbulence model is particularly effective for addressing supersonic flow problems involving high Mach numbers. Moreover, this model has demonstrated strong agreement with experimental data obtained from studies on steam ejectors. Consequently, it was selected as the turbulence model for the simulations conducted in this research [35–37]. The governing equations are as follows:

$$\frac{\partial}{\partial t}(\rho k) + \frac{\partial}{\partial x_i}[\rho k u_i] = \frac{\partial}{\partial x_i}\left[\left(\mu + \frac{\mu_t}{\delta_k}\right)\frac{\partial k}{\partial x_j}\right] + G_k + G_b - \rho\epsilon - Y_M \tag{3.7}$$

$$\frac{\partial}{\partial t}(\rho\epsilon) + \frac{\partial}{\partial x_i}[\rho\epsilon u_i] = \frac{\partial}{\partial x_i}\left[\left(\mu + \frac{\mu_t}{\delta_\epsilon}\right)\frac{\partial \epsilon}{\partial x_j}\right] + \rho C_1 S\epsilon - \rho C_2 \frac{\epsilon^2}{k+\sqrt{v\epsilon}} + C_{1\epsilon}\frac{\epsilon}{k}C_{3\epsilon}C_b \tag{3.8}$$

$$\text{with } C_1 = \max\left(\left[0.43, \frac{\mu}{\eta+5}\right]\right), \eta = S\frac{k}{\epsilon},$$

$$S = \sqrt{2S_{ij}S_{ij}}, S_{ij} = \frac{1}{2}\left(\frac{\partial u_i}{\partial x_j} + \frac{\partial u_j}{\partial x_i}\right)$$

$$\text{and } C_{1\epsilon} = 1.44, C_{3\epsilon} = 0.99, C_2 = 1.9, \delta_k = 1.0, \delta_\epsilon = 1.3.$$

Since the flow in an ejector is a wall-bounded problem, a proper near-wall treatment must be considered. In supersonic ejectors, the nature of the complexity increases significantly due to the interaction with the secondary stream. The secondary stream, initially moving at a very low velocity, flows along the ejector wall and gradually accelerates to supersonic speeds. During this acceleration process, it creates a resistance effect on the primary core flow, effectively generating a "shear stress layer interface. "This interaction leads to the occurrence of shear mixing, further complicating the flow dynamics within the ejector. The $k-\epsilon$ turbulence model is primarily designed for predicting turbulent core flows, typically in regions

away from the walls. Consequently, careful attention must be given to adapt or enhance these models to accurately address the wall-bounded flows. The challenge of addressing near-wall flow behavior is resolved through the implementation of the "Standard Wall Function". The literature suggests that the selected wall function is well suited for wall-bounded flows with significantly high Reynolds numbers [7].

3.3.2 Boundary Conditions

A set of boundary conditions are implemented following the reference study of Dong et al. [7]. The primary inlet is specified as the "Pressure inlet". Similarly, the secondary inlet is also set as "Pressure inlet". A "Pressure Outlet" boundary condition is specified at the outlet of the ejector. For the primary inlet, pressure is specified as 198.67 kPa with a corresponding saturation temperature value of 393.15 K. At secondary inlet pressure is 1.228 kPa with saturation temperature of 283.15 K. Condenser pressure and temperature are set as 1.0 kPa and 280 K, respectively. The ejector walls are thermally treated as adiabatic. Furthermore, there is no slip at the wall regarding velocity. An iterative solution process continues until convergence is achieved, meeting a residual threshold of 10^{-6} for all the solution variables.

3.3.3 Grid Independence

The accuracy of computational fluid dynamics (CFD) results is significantly influenced by the quality of the mesh utilized in the simulation. Using a too-coarse mesh can lead to inaccurate outcomes or, in certain cases, cause the solver to fail to converge. Conversely, employing an excessively fine mesh increases computational demands unnecessarily, resulting in inefficient use of resources and extended processing times. To identify the optimal mesh size that balances accuracy and computational efficiency, a grid convergence study is conducted. The study is carried out for the geometry presented in Figure 3.1 with $l_m = 60$ mm, Ma = 4.0 and NXP = 20 mm. Three mesh resolutions are used with 12000, 30900 and 56800 elements; these meshes are named as coarse, medium and fine, respectively. The

results of the Mach number are plotted along the centreline for the three mesh resolutions as shown in Figure 3.2. These plots qualitatively present the effects of the mesh refinement. It is observed that, for all three mesh resolutions, the Mach number plots in the primary nozzle and mixing chamber overlap showing no visible difference. The effects of mesh refinement, however, can be observed in the CAS and the diverging section of the ejector. At these sections, trends of Mach number converge as the mesh is refined. The results for the medium and fine grid resolution are almost identical suggesting the medium resolution grid is sufficient to proceed with.

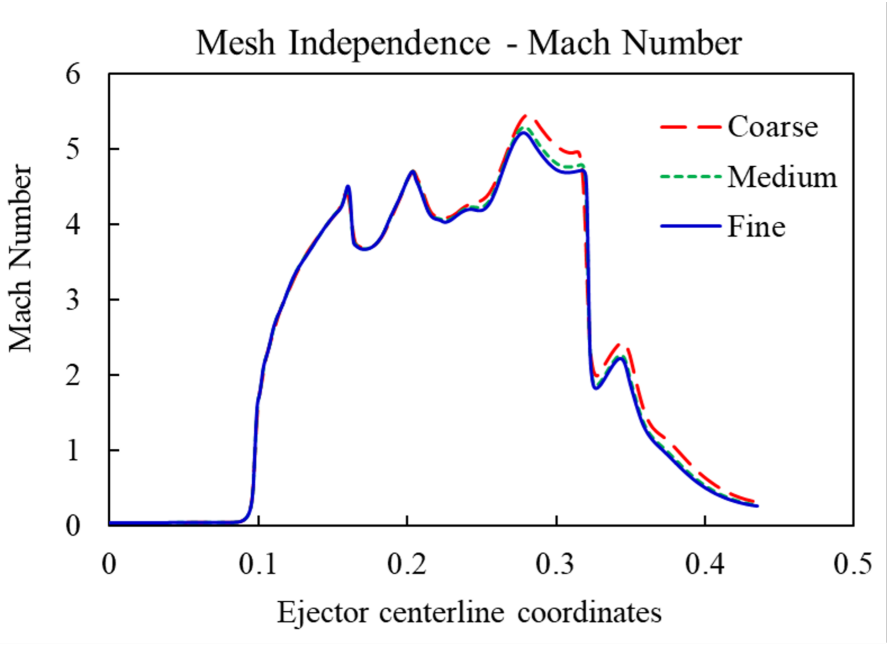

FIGURE 3.2: Mesh convergence results showing the Ma plots at centerline of an ejector using three mesh resolutions

To quantitatively analyze the effects of mesh refinement, the entrainment ratio values for the three grids are compared as shown in Table 3.3. The difference in ω values decrease as the mesh is refined. It can be seen that the difference between the ω values of coarse and medium meshes is 2.05% which reduces to 0.25% when the results of medium and fine meshes are compared. It also justifies medium resolution grid as good enough for the rest of the simulations.

3.4 Validation of Numerical Solution Procedure

A validation study is performed to verify the correctness of the results obtained from the numerical solution strategy employed in this research. For this purpose,

TABLE 3.3: Mesh convergence data showing the % difference in the values of the entrainment ratio

Mesh	**Entrainment Ratio**	**% Difference**
Coarse	0.52896	-
Medium	0.53985	2.05
Fine	0.54124	0.25

the benchmark study by Dong et al. [7] is utilized as a reference for comparison. The geometrical variables used in the validation are: constant area section length $l_c = 55\,\text{mm}$ and the diffuser section length $l_d = 200\,\text{mm}$, and Ma = 3.0. The l_m is varied systematically from 0 to 120 mm with increments of 20 mm. Key performance metrics analyzed during the validation are the p_{cr} and ω.

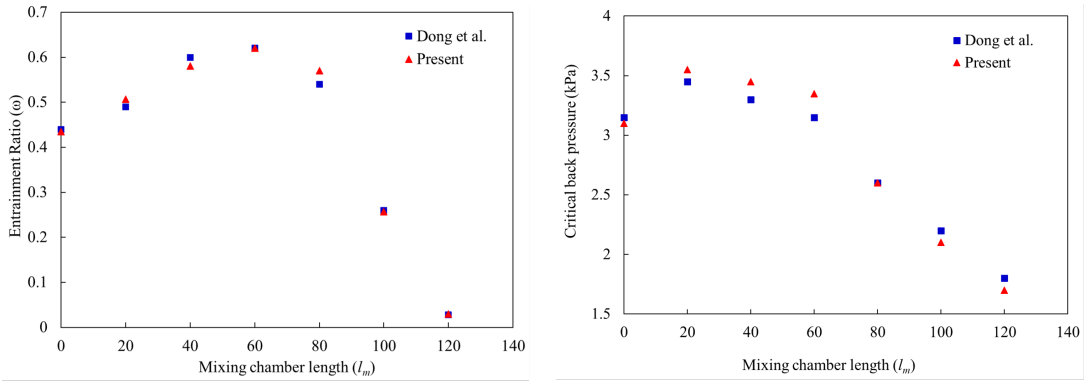

(a) (b)

FIGURE 3.3: Validation study – (a) ω and (b) p_{cr} of the present numerical study compared with the results of Dong et al. [7] for various mixing chamber lengths

Figure 3.3 illustrates a comparison of the numerical results obtained in this study with those reported by Dong et al. for both performance parameters. An excellent agreement between the two results is observed for the ω (Figure 3.3(a)) and p_{cr} (Figure 3.3(b)), which justifies the validity of the numerical procedure applied for solving this compressible flow problem.The Minor differences observed between the two studies are attributed to the difference in the simulation approaches used in the respective studies.

Dong et al. performed simulations using a three-dimensional (3D) ejector model, assuming symmetry along the central plane and solving only half of the geometry. Conversely, the present study modeled the ejector as a two-dimensional (2D) axisymmetric structure. The close alignment of the results of the present study

against the benchmark case of Dong et al. not only confirms the reliability of the numerical approach but also validates the simplification of treating the 3D ejector as a 2D axisymmetric model. This approach significantly reduces computational costs without compromising the accuracy of the results, demonstrating its practical utility in simulating such systems.

Chapter 4

Results and Discussion

The present study conducts a computational analysis to examine the effects of varying the position of primary nozzle in the mixing chamber on the steam ejector performance. The analysis is performed for two l_m values: 20 and 60 mm, and four Ma values: 2, 3, 4, and 5. The geometry of ejector and operational conditions are based on the work of Dong et al. [7], who explored the effects of l_m on the performance indicators ω and P_{cr} of an ejector applied in a steam refrigeration system. The performance parameters evaluated in the current study also include ω and P_{cr}. Schematic of an ejector highlighting geometric variables under investigation is shown in Figure 4.1. The details of the numerical experiments conducted in this study are listed in Table 4.1. A total of 80 geometries were created for this investigation. To determine the P_{cr}, each geometry is iterated by varying the condenser pressure until the ω value drops below a stable value of the double choking mode.

TABLE 4.1: Geometric variables and their numerical values investigated in this study

Mixing chamber length (l_m)	**Mach Number (Ma)**	**Primary Nozzle Exit Position (NXP)**	**Number of geometries**
20 mm	2, 3, 4, 5	For each Ma number: -15, -10, -5, 0, 5, 10, 15, 20, 25	$9 \times 4 = 36$
60 mm	2, 3, 4, 5	For each Ma number: -30, -20, -10, 0, 10, 20, 30, 40, 50, 60, 70	$11 \times 4 = 44$
Total geometries			**80**

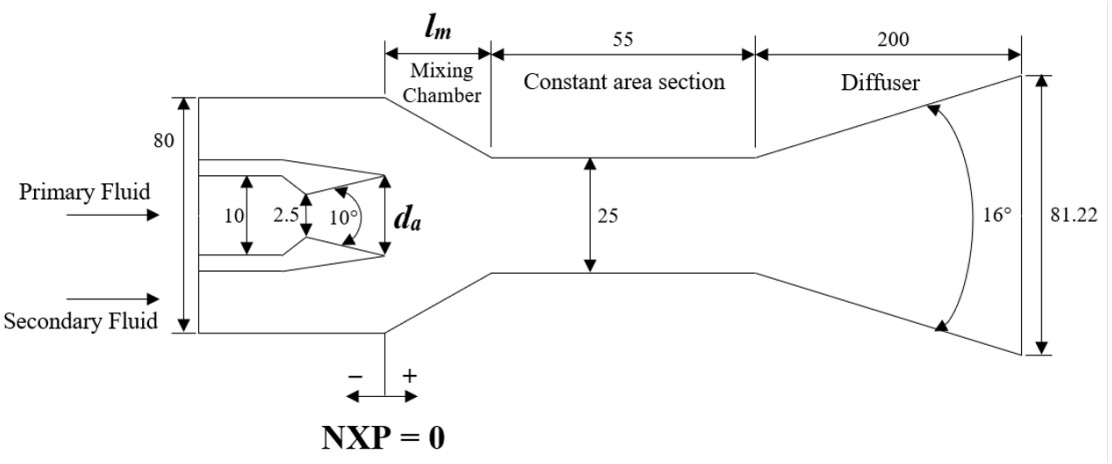

FIGURE 4.1: Schematic diagram of the object ejector geometry. The fixed geometric dimensions (in mm) are mentioned numerically on the figure. The variable geometric parameters are mentioned using the symbols-details are mentioned in Table 4.1

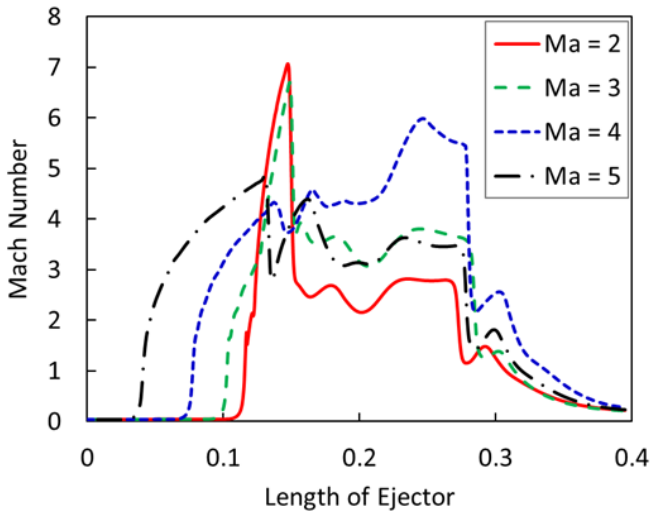

FIGURE 4.2: The line plots of Ma number plotted against the length of the ejector along the centreline for all the Ma number cases. The plots are generated for NXP = 0 for all the cases.

4.1 Variation of Entrainment Ratio with NXP

4.1.1 l_m = 20 mm

It is important to first analyze the state of expansion in the primary nozzle for different Ma numbers cases because it dictates the shock train generated at the exit of the primary nozzle. This ultimately governs the entrainment of the secondary fluid and therefore the performance of the ejector. Figure 4.2 presents the line plots of the Ma number plotted along the centreline of the ejector for all the Ma

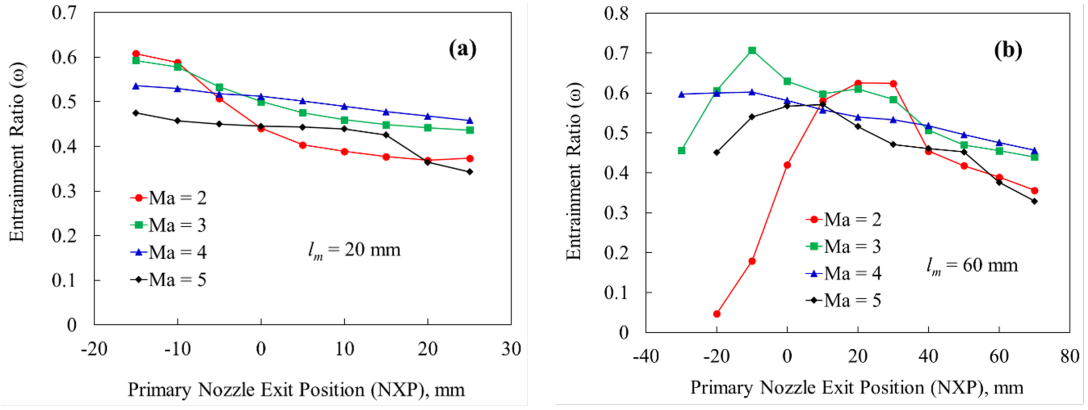

FIGURE 4.3: Line plots of the entrainment ratio for all the Ma number cases plotted against the exit position of the primary nozzle (NXP) for (a) l_m = 20 mm and (b) l_m = 60 mm

number cases at NXP = 0. It can be seen that Ma = 2 is a case of strong under expansion. The fluid continues to expand as soon as it exits the primary nozzle. A spike of the Ma number is observed at the exit of the primary nozzle attaining Ma number value of as high as 7.4. This is followed by a strong oblique shock and a series of oblique shocks and expansion waves as the flow continues its journey in the constant area section and the diffuser. The Ma = 3 is also a case of under expansion and fluid continues to expand outside the primary nozzle achieving Ma value of 7. However, the strength of the oblique shock after the expansion fan is a bit weaker as compared to Ma = 2, and the flow maintains comparatively high Ma number throughout the ejector. The case of Ma = 4 is a case of slight under expansion or approximately complete expansion. The maximum Ma number at the primary nozzle exit is 4.25. The fluid continues to gain momentum in the constant area section and a strong shock is produced in the diffuser section, compressing the fluid. It is interesting to note that the average Ma number in the ejector is maximum for Ma = 4 case. Finally, for Ma = 5, the fluid overexpands in the primary nozzle. Therefore, as the fluid exits the primary nozzle, strong shocks are encountered reducing the Ma number to 3.

Figure 4.3 presents plots of the entrainment ratio for l_m = 20 mm and l_m = 60 mm for all values of Ma numbers and NXP positions. The plots for l_m = 20 mm are shown in Figure 4.3(a). For Ma = 2, the entrainment ratio decreases as the NXP value is increased by translating the primary nozzle from the inlet of the ejector to the exit of the ejector. At NXP = −15 mm, the ω is maximum reporting a

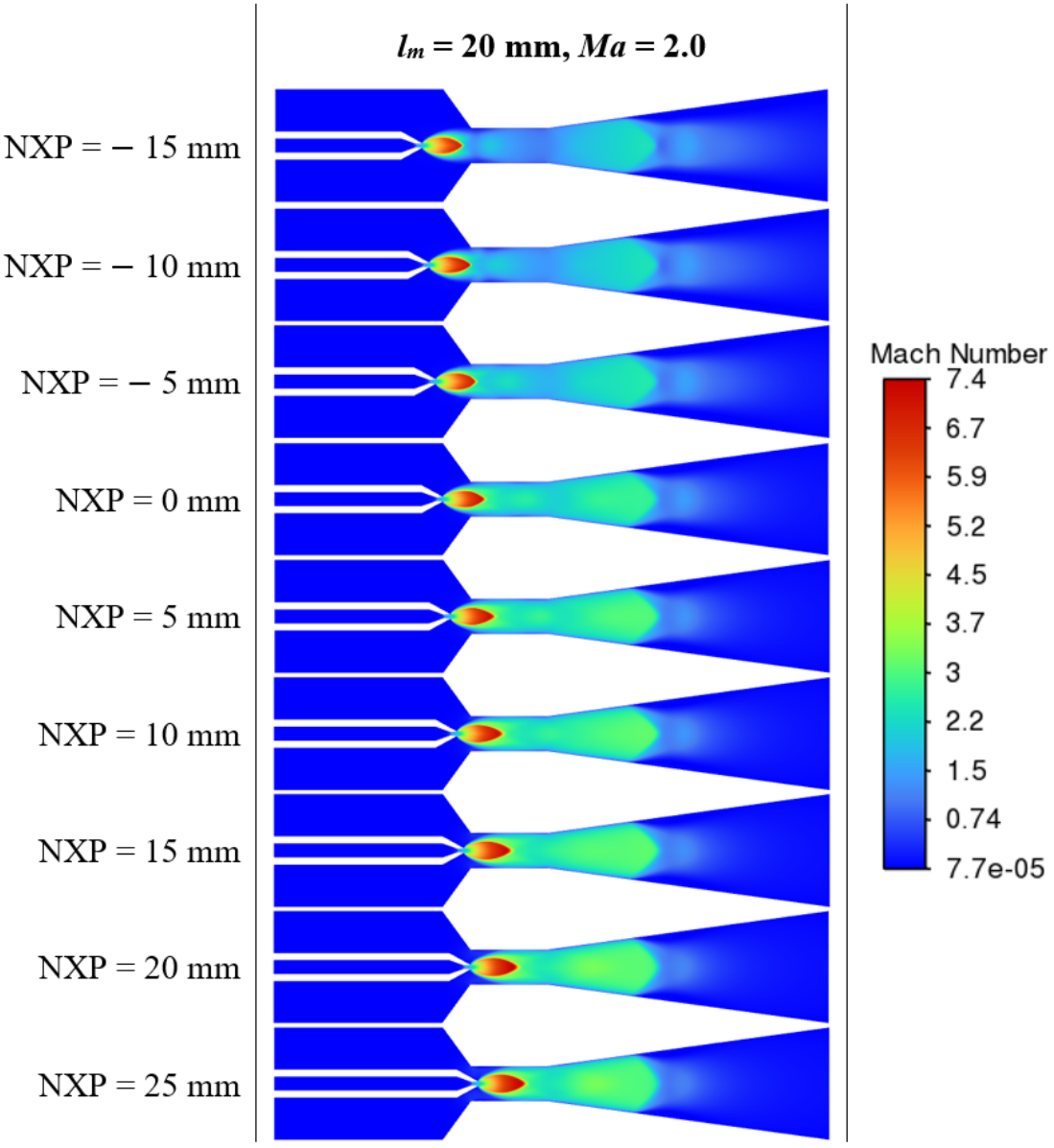

FIGURE 4.4: The contour plots of Mach number for Ma = 2 case for l_m = 20 mm and varying NXP values

value of 0.607. It decreases a bit for NXP = −10 mm and then sharply decreases till NXP = 5 mm. Afterwards, it stays almost constant till NXP = 25 mm. To explain this trend, the contour plots of Mach number are presented in Figure 4.4 for all values of the NXP.

It is observed that the primary flow emitting out of primary nozzle makes an expansion fan with high Ma number values. The maximum value of Ma number is approximately 7.4. It indicates that this is the case of an under-expanded nozzle and the fluid continues to expand as it flows out of the primary nozzle. The Ma

number values and the size and shape of the expansion fan are crucial in explaining the trends of the entrainment ratio in the ejector. This is because the expanding jet emitted from the primary nozzle will decide effective space for the flow of secondary steam. Furthermore, the flow velocities will dictate the pressures at the primary nozzle exit and will generate suction force for entrainment of secondary steam. From the Ma number contours, it can be seen that For NXP $= -15$ mm, the expansion fan is away from the fixed area section allowing sufficient space for the flow of entrained steam. Additionally, the high velocities create low pressures to generate high suction force to entrain the secondary vapor. This is also obvious from the contours of pressure gradients plotted for $l_m = 20$ mm and Ma $= 2.0$ case as shown in Figure 4.5. High pressure gradients exist at the entry of the constant area section. Both these factors contribute positively to entrain large amounts of secondary vapor and give high entrainment ratio values. It must be noted that the primary mass flow rate is dictated by the throat area of the primary CD nozzle and generator pressure and stays constant throughout this study. Now, as CD nozzle is moved toward the fixed area section, high-velocity flow in the primary expansion fan interacts with the ejector geometry and reduces space for entrainment of secondary vapor. This phenomenon continues till NXP $= 5$ mm because at this position the maximum width of the expansion fan is at entrance of fixed area section. This represents the maximum blockage to the flow of the secondary vapor and the entrainment ratio is reported as 0.4. This also corresponds to the minimal value of pressure gradient at the entry of the constant area section. For further values of NXP, the entrainment ratio values almost stay constant since the maximum blockage has entered the constant area section allowing a fixed space for secondary stream.

The contours of density gradient are presented for $l_m = 20$ mm and Ma $= 2$ case in Figure 4.6. The large values of density gradients indicate the location of shocks. The shocks are created at the primary nozzle exit around the expansion fan and inside the diffuser section. The shock structures significantly change as the NXP value is changed. It is important to note that as the NXP value is increased by moving the primary nozzle towards the constant area section, the shock structure enters the constant area section, however, the location of secondary shock in the

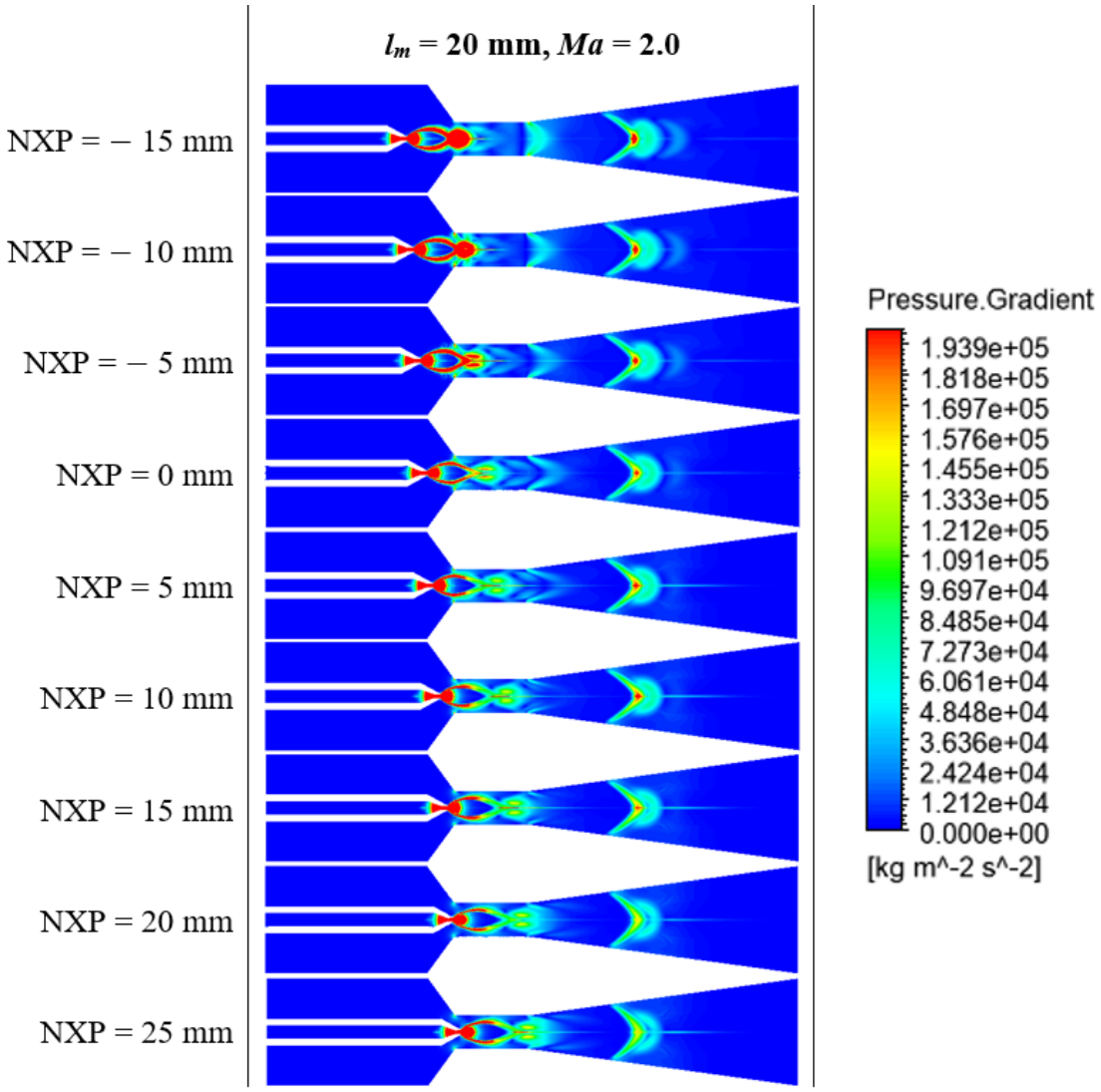

FIGURE 4.5: The contour plots of pressure gradient for Ma = 2 case for l_m = 20 mm and varying NXP values

diffuser section almost stays fixed. Hence, the length of shock train decreases with an increase in NXP. Furthermore, the strength of shock wave generated in the diffuser section increases by increasing the NXP value.

The contours of static temperature are presented in Figure 4.7 for varying values of NXP. A very low temperatures are observed in the expansion bulb generated at the exit of the primary nozzle. This is because most of the energy is converted into the kinetic energy reporting Ma number of 7.4. Consequently, as the shocks are generated, velocity decreases and the temperature increases. Therefore, the trends of increasing-decreasing temperatures correspond to the location of shock and expansion waves in the shock train. In the diffuser section, the temperature instantly increases after the ¿-shaped oblique shocks. The flow becomes subsonic afterwards

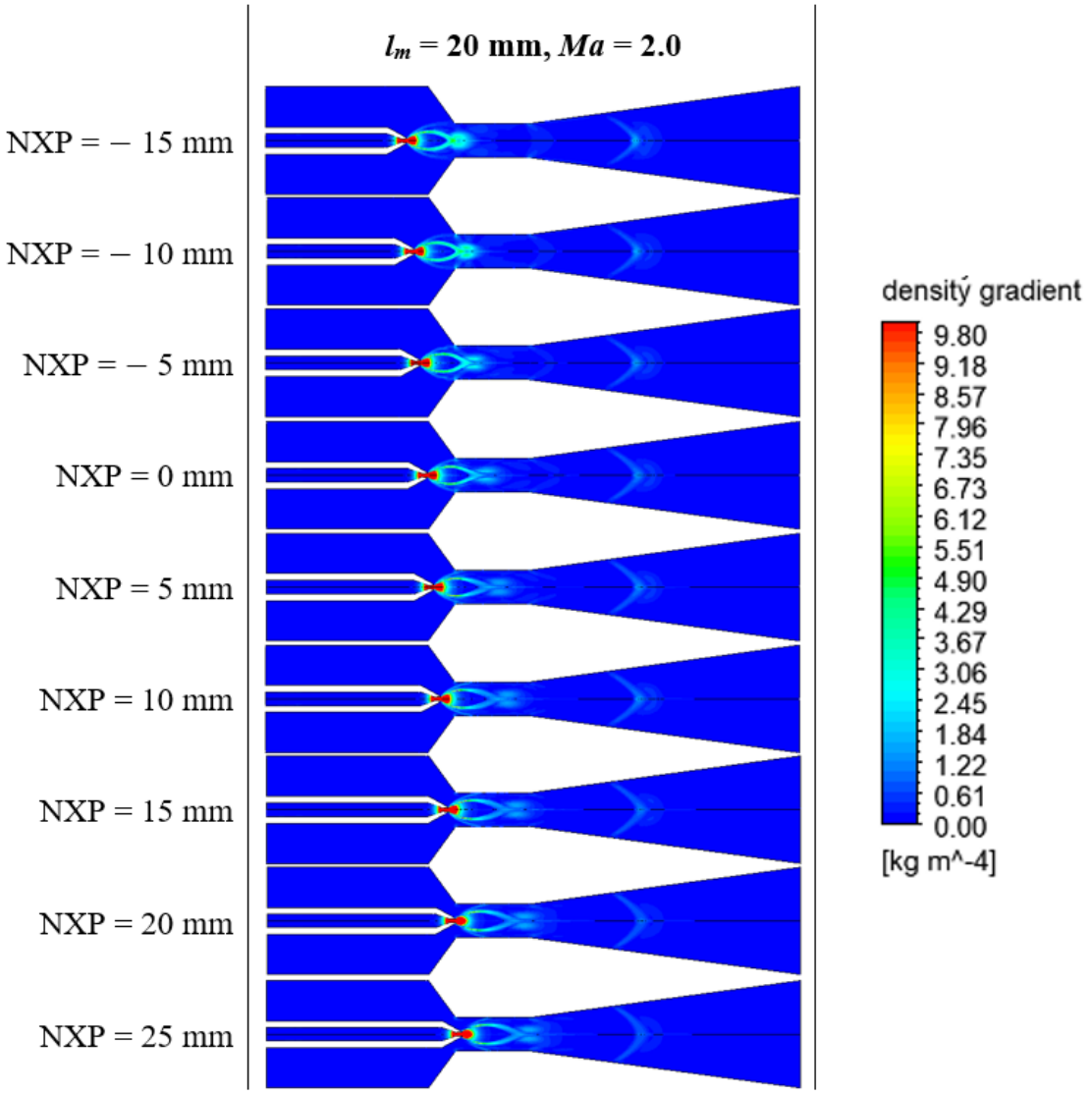

FIGURE 4.6: The contour plots of density gradient for Ma = 2 case for l_m = 20 mm and varying NXP values

and continues to decelerate in the diffuser section resulting in an increase in the static temperature of the fluid.

Plots of ω for Ma = 3, shown in Figure 4.3(a)., presents similar behavior as for the Ma = 2 case: starts at almost the same values for NXP = −15 mm, and decreases as the NXP is increased. However, the ω values are greater than those for Ma = 2 case. To explain this, the Mach number contours are presented in Figure 4.8 for all values of NXP.

It can be observed that for Ma = 3, primary stream is still under-expanded, therefore, the rest of the expansion takes place after exiting from the CD nozzle making an expansion fan at the exit plane. The under expansion for Ma = 3

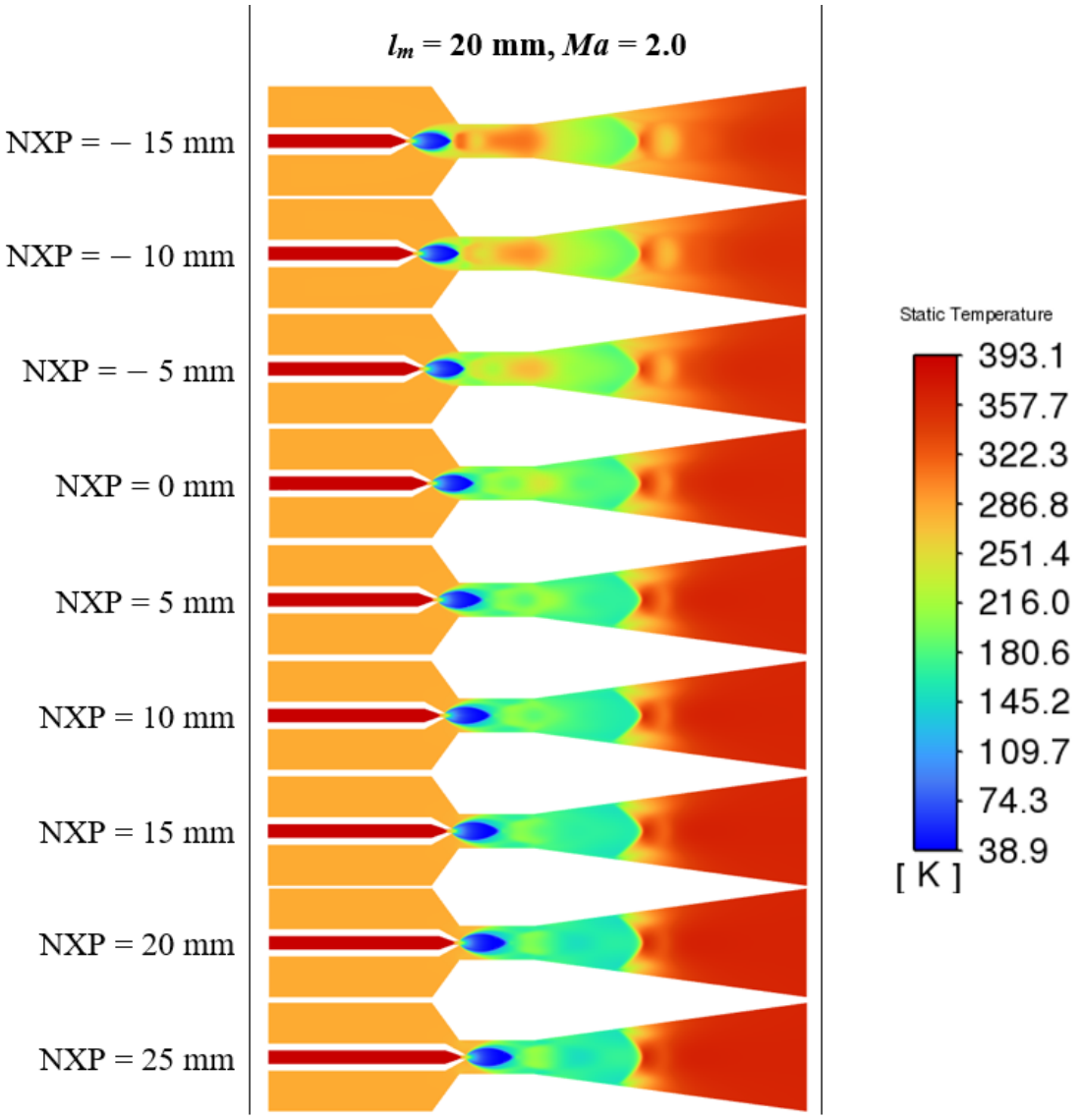

FIGURE 4.7: The contour plots of density gradient for Ma = 2 case for l_m = 20 mm and varying NXP values

is however, lesser than for Ma = 2 case and therefore the width and size of the expansion fan will be smaller and will offer lesser hindrance to the secondary flow as compared to the Ma = 2 case. Consequently, when the primary nozzle approaches the constant area section and expansion fan enters that space, it makes available more area for the entrainment of the secondary fluid resulting in higher values of entrainment ratio for NXP values of −5 mm and above. Furthermore, since the primary nozzle exit Ma number is high, therefore, lower pressures will be created to suck the secondary vapor into the mixing chamber as compared to Ma = 2. This also contributes towards increasing the value of ω for Ma = 3. The ω values for Ma = 4 smoothly decrease with quite a low slope as the NXP value is varied between

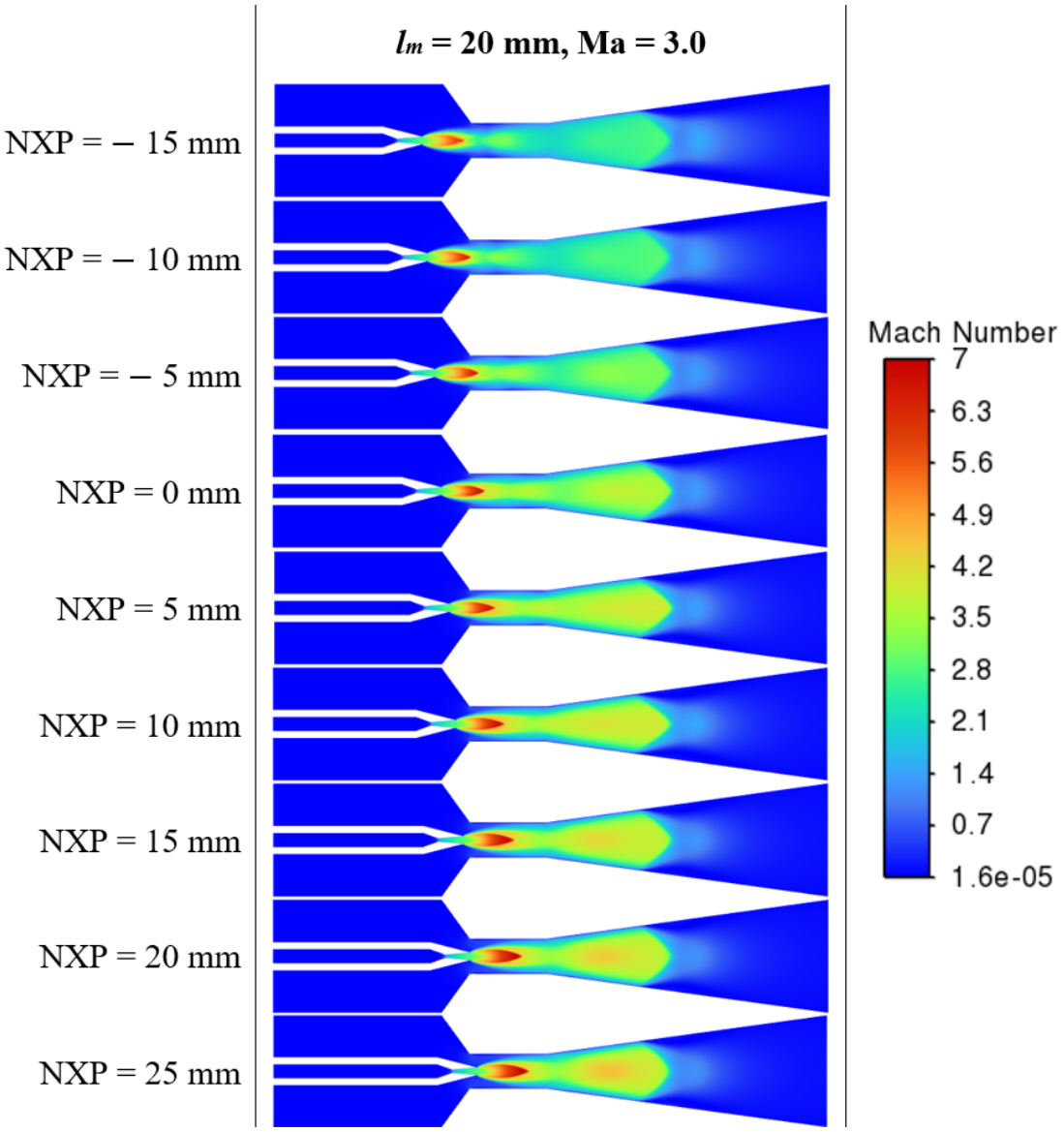

FIGURE 4.8: The contour plots of Mach number for Ma = 3 case for l_m = 20 mm and varying NXP values

-15 mm and 25 mm. Except for NXP = 15 mm and −10 mm, the entrainment ratio is higher than that of the Ma = 2 and 3 cases. To understand this behavior, the contours of the Ma number for Ma = 4, presented in Figure 4.9, need to be explored. It is observed that the primary jet leaves the CD nozzle with a small amount of under-expansion. The maximum value of Ma is approximately 4.2 at the exit of the primary nozzle.

This means that this nozzle design is approximately a perfect choice for the set operating conditions. There is a negligibly small expansion fan generated at the exit plane of the primary nozzle. Therefore, hindrance to the entrained vapor

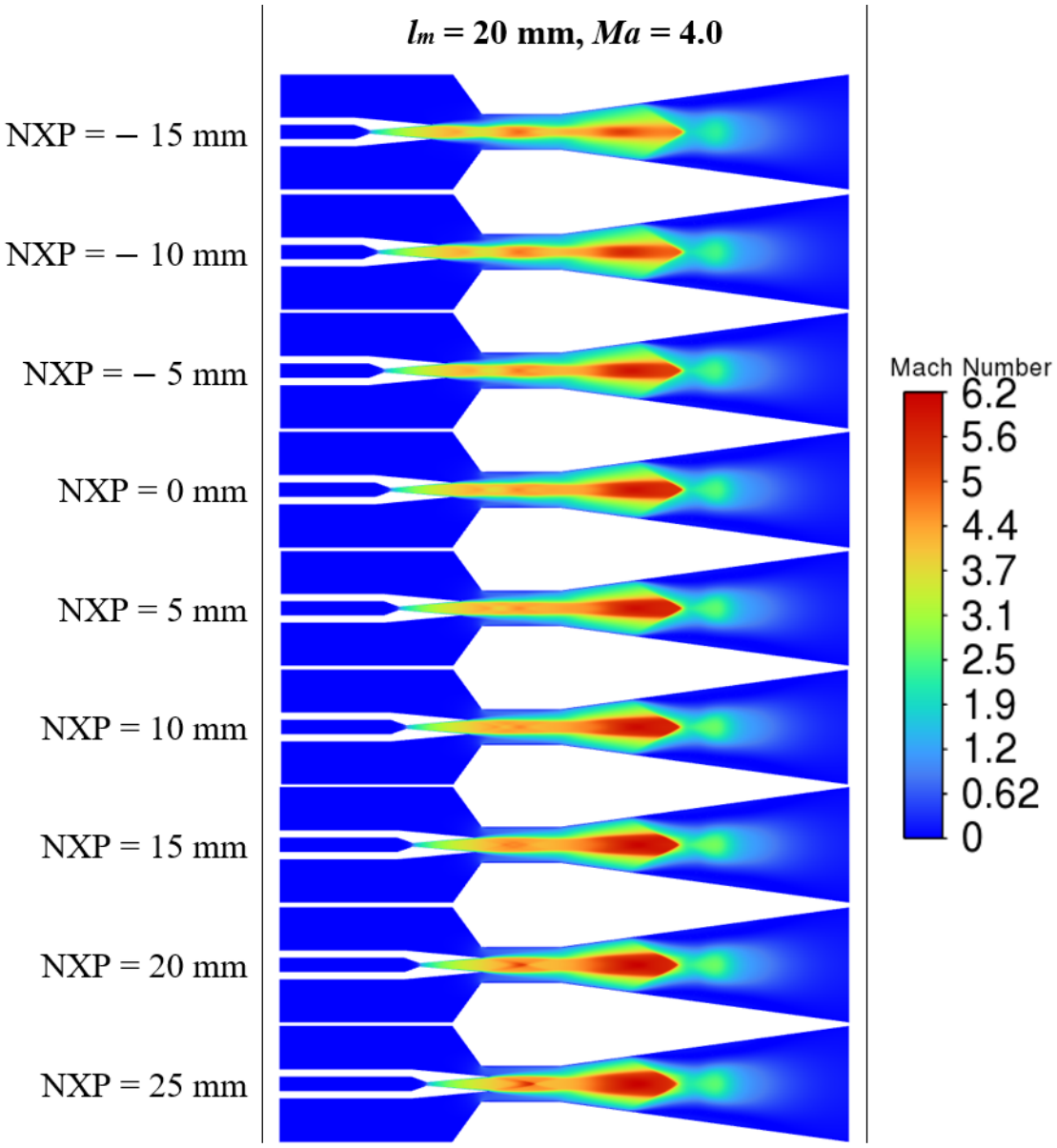

FIGURE 4.9: The contour plots of Mach number for Ma = 4 case for l_m = 20 mm and varying NXP values

reduces since obstruction that was previously created by the expansion fan is no more here. However, it must be noted that the outlet diameter of the CD nozzle increases as Mach number at nozzle exit is increased through Ma = 2 – 5. This causes a reduction in the allowable space for the flow of entrained vapor as the NXP value is increased. However, its magnitude, for Ma = 4 is lower as compared to the width of the expansion fan created by Ma = 2 and Ma = 3 cases. Therefore, the entrainment ratio decreases as the NXP is increased but with a smaller slope.

For Ma = 5, the entrainment ratio stays approximately constant for NXP as it is varied through -15 mm to 15 mm. Afterward, there is a decrease in the entrainment

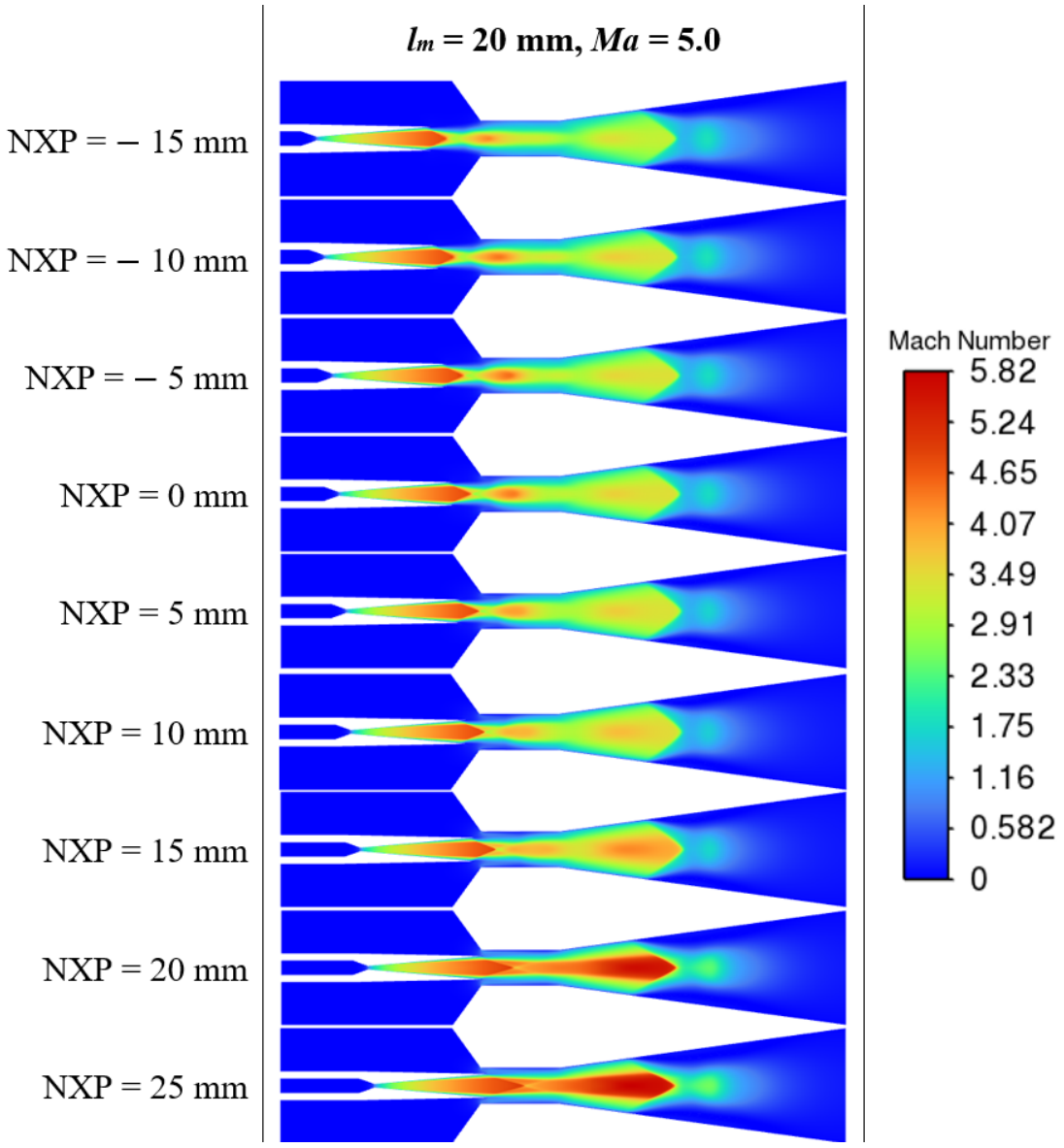

FIGURE 4.10: The contour plots of Mach number for Ma = 5 case for l_m = 20 mm and varying NXP values

ratio for NXP = 20 mm and 25 mm. The contour plots of Mach number for Ma = 5, presented in Figure 4.10, show that this nozzle design gives an over-expanded primary jet, and therefore shock waves are created right at the exit plane of the primary nozzle. An expanded structure of the shock diamond follows these shock waves. That particular shock diamond stands at the inlet plane of the fixed area sectionof the ejector. Since the observed shock diamond creates limiting effective entrainment space for secondary vapor, and it lies at the entry of CAS for NXP = −15 mm and will travel further into the constant area section for rest of the NXP values so the secondary flow and ω stay constant till NXP = 15 mm. For NXP = 20 mm, the primary nozzle exit is at the entrance plane of fixed area

region. For Ma = 5, the exit diameter of CD nozzle is 16.4 mm while the diameter of the fixed area section is 25 mm leaving a peripheral space of 4.5 mm for the flow of secondary vapor. Due to this blockage, the entrainment ratio is suddenly decreased for NXP = 20 mm and 25 mm.

4.1.2 l_m = 60 mm

The line plots of the entrainment ratio for l_m = 60 mm and Ma = 2, 3, 4 and 5 are presented in Figure 4.3(b) for NXP values in the range −30 mm – 70 mm. It is observed that for Ma = 2, 3 and 5, the ω values first increase followed by a decreasing trend. For Ma = 4, however, there is a continuously decreasing trend in the entrainment ratio values as the NXP value is increased. To understand the physics of these trends, the contours of Mach number are presented in Figure 4.11 for Ma = 2 for all the studied NXP values.

For Ma = 2, the entrainment ratio is approximately zero at NXP =−20 mm. This is because the shock train generated in the primary steam jet exiting from the primary nozzle is so configured that the low velocity and correspondingly high-pressure region positions at the entry plane of the CAS. This effectively blocks entrainment of secondary vapor and therefore the entrainment ratio approaches to zero. Furthermore, this is the case of an under-expanded nozzle and significantly high Ma numbers are generated as the fluids expand outside the primary nozzle in the mixing chamber. Correspondingly, strong shocks are produced in the shock train which significantly reduces the Ma number and increases the pressures in the mixing chamber. This eventually decreases the pressure difference between the secondary stream and the mixing chamber, reducing suction force for the entrainment of the secondary vapor stream. When primary nozzle is advanced towards fixed area section, shock train also shifts towards that region. This brings high-velocity/low-pressure region of the shock train near the entrance of the CAS. As a result, suction effect increases resulting in an increase in the value of ω. The increasing trend is visible as sharp rise in entrainment ratio values as the NXP varies through −10 mm – 10 mm. When the primary nozzle is further moved in the positive direction till NXP = 30 mm, the entrainment ratio continues to increase

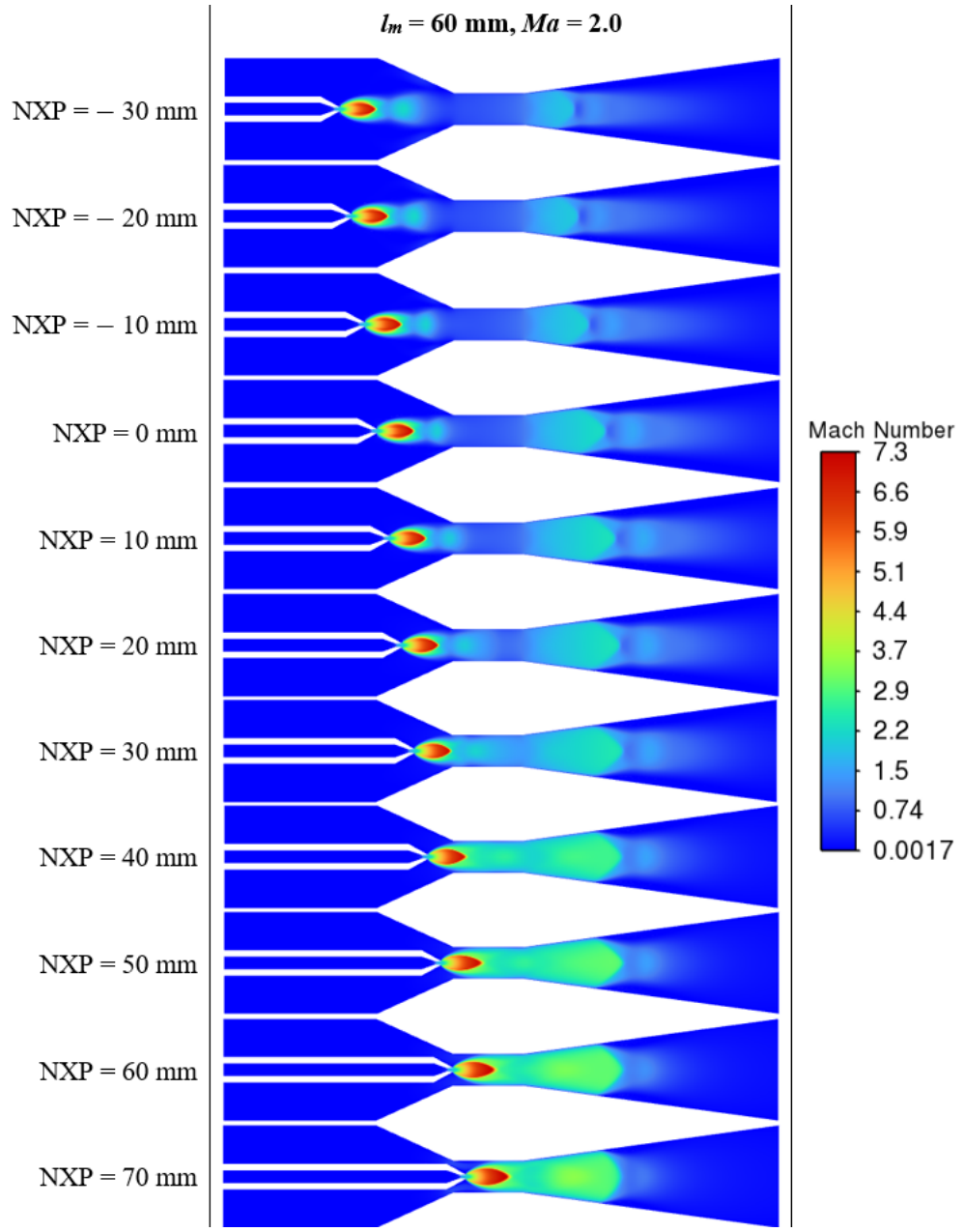

FIGURE 4.11: The contour plots of Mach number for Ma = 2 case for l_m = 60 mm and varying NXP values

but the increase is quite small. At NXP = 40 mm, the primary nozzle is so placed that maximum width of the high momentum steam jet expansion fan is at the entrance of CAS. As a consequence of this, the area available for the entrainment of the secondary vapor stream decreases, resulting in a sharp reduction in the value of ω.

As NXP is further increased to 50 mm, 60 mm and 70 mm, the entrainment ratio continues to decrease at a constant slope. This is because most of the CAS is occupied by high-momentum main fluid stream. The additional restriction to the

flow of the secondary stream is imposed by the physical interaction as the primary nozzle geometry comes close to the constant area section. At NXP = 70 mm, the peripheral space for the flow of secondary vapor is quite small restricting the entrainment secondary entrainment and decreasing the entrainment ratio.

For the Ma = 3 case, at NXP = −30 mm through 0 mm, the values of the entrainment ratio are quite high as compared to Ma = 2 case. This is because the Ma = 3 case is less under-expanded as compared to Ma = 2 and therefore the Ma numbers in the shock train, shown in Figure 4.12, are lower than that of the Ma = 2 case. This will produce weaker shock waves in the shock train consequently maintaining significantly high velocities and low pressure throughout as compared to Ma = 2 case. Therefore, the suction effect generated entrains more secondary vapor resulting in large values of entrainment ratio. The top value of ω is reported as 0.707 at NXP = −10 mm which is the highest among all the cases studied in this research. After attaining the maximum value, the entrainment ratio decreases, increases, and then decreases continuously afterward. These fluctuations are due to two reasons. First, the low-pressure and high-pressure regions of the shock train successively pass through the inlet of the CAS affecting entrainment of secondary vapor. Second, the interaction of the expansion and contraction regions of the shock train with the constant area for entrainment of vapor from the evaporator and eventually ω. At NXP = 30 mm, the first expansion fan of the shock train starts entering constant area section. Therefore, ω continuously decreases as soon as expanded region enters the constant area section. Finally, at NXP = 70 mm and beyond, the physical interaction of the convergent divergent primary nozzle and the CAS becomes a dominant source of obstruction for the flow of the steam from the evaporator.

The Case of Ma = 4 is quite smooth as compared to all other Ma number cases as it shows a continuous decreasing trend in the values of the entrainment ratio for NXP variation in the range −30 mm – 70 mm. This smooth variation is primarily due to the fact that the Ma = 4 is a case of approximately complete expansion or a slight under-expansion. Therefore, the expansion and contraction regions are of very small magnitude and minutely affect the available space for entrainment of steam from the evaporator. A continuous decreasing trend is attributed to the

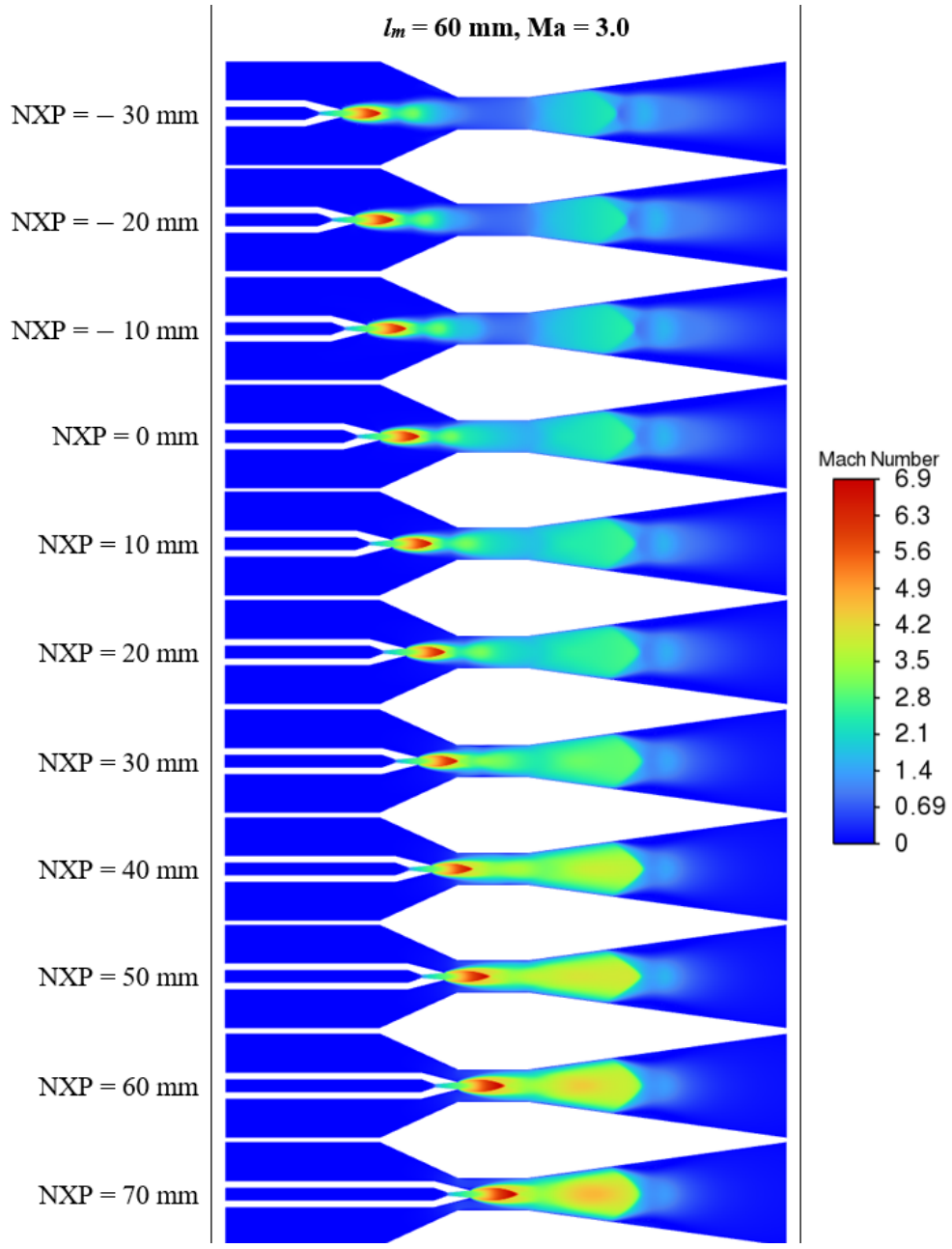

FIGURE 4.12: The contour plots of Mach number for Ma = 3 case for l_m = 60 mm and varying NXP values

progressively increasing pressures and decrease in the available space for entrainment of the vapor stream from the evaporator as primary nozzle approaches the CAS. As primary nozzle enters the CAS for NXP = 70 mm, the physical space for the secondary vapor entrainment further decreases maintaining the decreasing trend of ω. Contours of the Mach number for Ma = 4 are shown in Figure 4.13.

For the case of Ma = 5, the primary nozzle is over-expanded. Therefore, oblique shock is produced right at the primary nozzle exit followed by an expansion fan

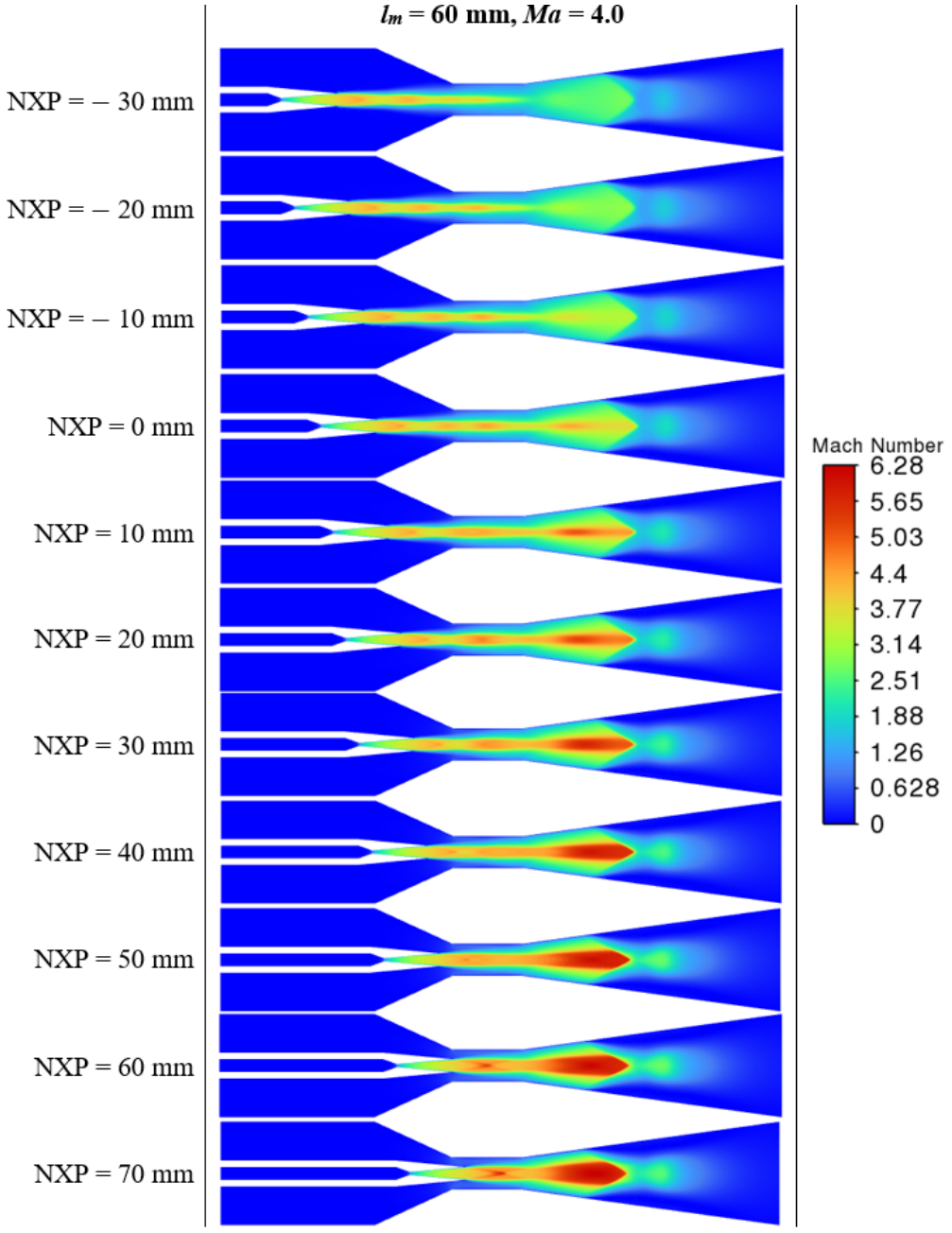

FIGURE 4.13: The contour plots of Mach number for Ma = 4 case for l_m = 60 mm and varying NXP values

and subsequent shock train presented Figure 4.14. Therefore, the entrainment ratio trends show periodic increasing and decreasing patterns. This is because of the change in the effective area available for the entrainment of secondary vapor as the expansion and contraction sections of the shock train interact with the CAS.

A sharp decline in the entrainment ratio at NXP = 60 mm is observed when the exit of the primary nozzle is situated at the entry plane of the constant area section. This is because of the very narrow physical space for the flow of secondary vapor.

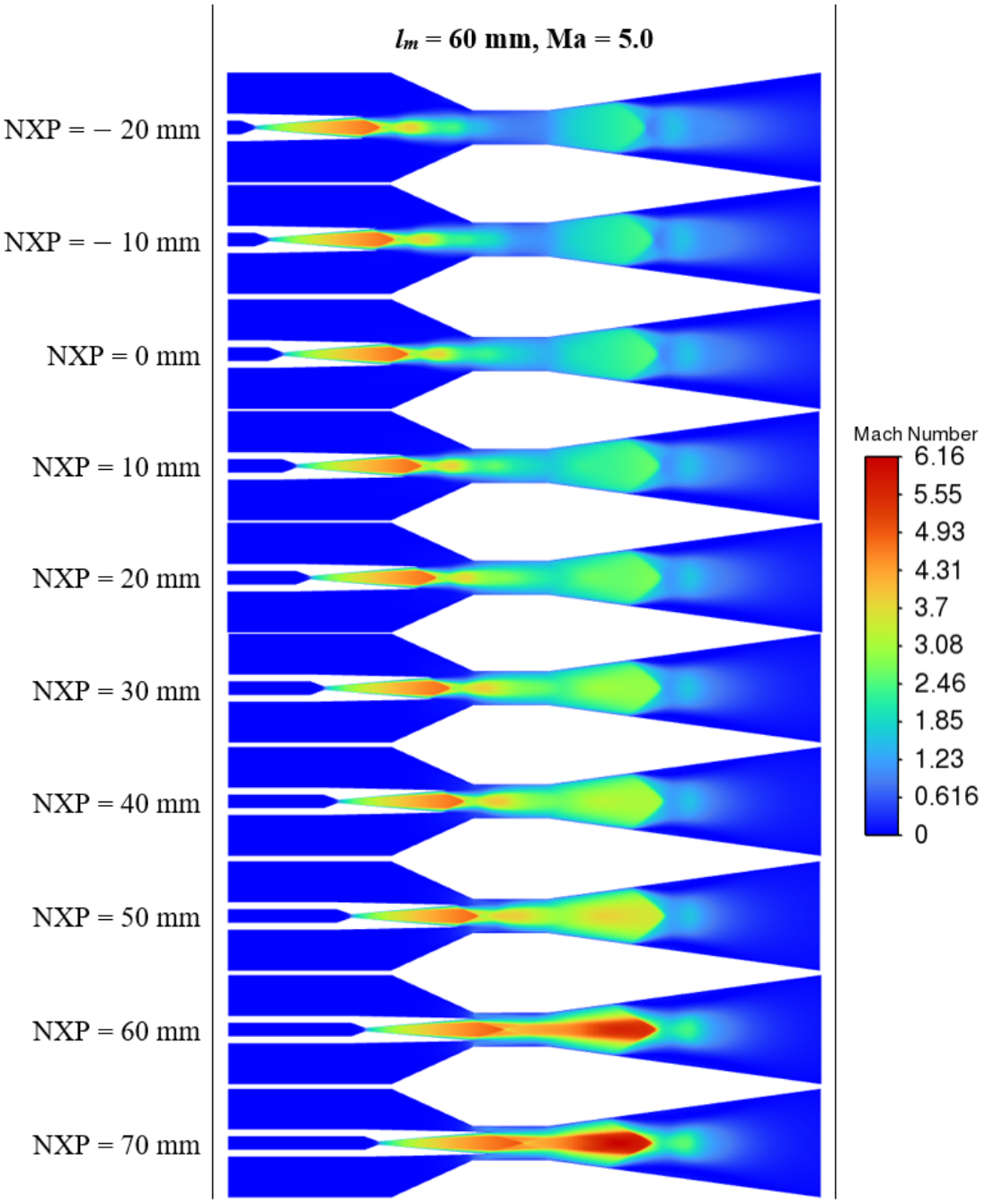

FIGURE 4.14: The contour plots of Mach number for Ma = 5 case for l_m = 60 mm and varying NXP values

This condition becomes more restrictive when exit of the convergent divergent nozzle is placed within the CAS for NXP = 70 mm.

4.2 Variation of Critical Back Pressure with NXP

Another important performance parameter is the critical back pressure which is the limiting value of the condenser pressure for which the ejector operates in the

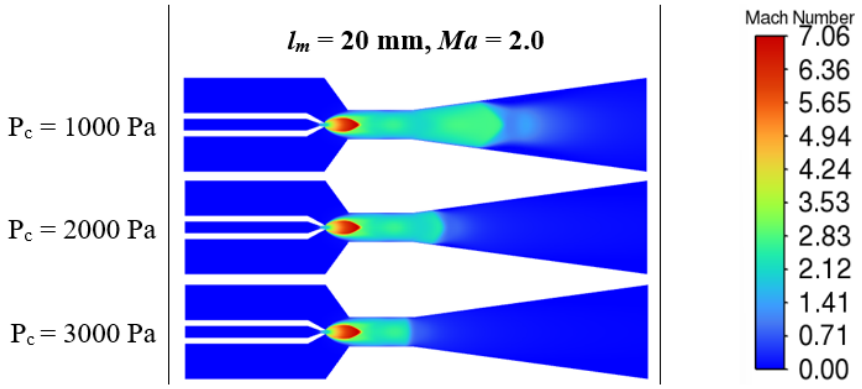

FIGURE 4.15: The contours of Ma number plotted for varying values of condenser pressure

double choking mode. If the condenser pressure is greater than the critical back pressure, the ejector will no more be operating in the double choking mode and the performance of the ejector and the refrigeration system will drastically decrease. This is due to the fact that an increase in the condenser pressure will push the shock waves back into the mixing section and disturbs the flow of primary and secondary streams. This is explained with the help of contours plots of Ma number for different values of condenser pressure as shown in Figure 4.15. Initially, the condenser pressure in 1000 Pa and the ejector operates in the double-choking mode producing maximum entrainment ratio and the primary and as well as diffuser shocks. When the condenser pressure is increased to 2000 Pa, the ejector still operates in double-choking mode and with maximum entrainment ratio, however, shock structure is changed and in pushed into the constant area section. Now, as the condenser pressure in further increase to 3000 Pa, the ejector is still in double choking mode, but the shock is further pushed back into the mid of the constant area section. Now if the pressure is further increased, it may further push the shock into the mixing section and the double-chocking mode will no longer exist. For this particular case, the critical back pressure is 3300 Pa. Therefore, if the condenser pressure is increased beyond 3300 Pa, the ejector will no more be in double-choking and will become unstable.

4.2.1 l_m = 20 mm

The critical back pressure is plotted against NXP for different values of Ma and for both $l_m = 20\,\text{mm}$ and $l_m = 60\,\text{mm}$ in Figure 4.16. For $l_m = 20\,\text{mm}$ results

are shown in Figure 4.16a. It can be seen that P_{cr} for Ma = 2 rises as NXP is increased and tends to become constant after NXP = 10 mm. For the rest of the Ma number cases, the critical back pressure predominantly shows a decreasing trend throughout as the NXP is increased. These trends are linked to the under-expansion and the over-expansion phenomena observed at the primary CD nozzle exit for different Ma number cases. This under-expansion and over-expansion are then linked to the momentum of the fluid moving along the ejector. The momentum of the fluid stream in the ejector is also significantly affected by the shock train generated at the primary nozzle exit as well as shock waves generated at the start of diverging section of the ejector.

The Ma = 2 case is a case of strong under-expansion. Therefore, the fluid coming out of the primary nozzle expands outside the nozzle achieving high Ma number (7.5). This produces strong shocks in the primary shock train and significantly reduces the flow momentum in the ejector (Figure 4.4). For NXP = −15 mm, the length of the shock train is larger, and the expansion bulb is away from the CAS and lies in the mixing chamber. Consequently, the momentum fails to build up in the CAS leading to a comparatively lower value of P_{cr}. As the NXP value is increased, expansion bulb starts entering the CAS and length of shock train gets smaller. In the CAS, momentum builds up increasing the P_{cr}. However, in doing so, strength of secondary shock also increases which may negatively impact the critical back pressure. For Ma = 3, there is under-expansion as well, however, it is of less magnitude as compared to the Ma = 2 case. Therefore, the strength of shock waves in the shock train are lesser comparatively resulting in an increased momentum of the fluid stream. However, this increased momentum results in stronger secondary shock waves in the diffuser section and their strength increases as the NXP values are further increased (Figure 4.8). Therefore, critical back pressure continuously decreases as the primary nozzle is moved towards the CAS.

A similar decreasing trend is observed for the Ma = 4 which is again a case of slight under-expansion. The secondary shock gets stronger as the NXP is increased as shown in the contour plots of Ma number in Figure 4.9. The Ma = 5 is the case of over-expansion and the length of the primary shock train is significantly shorter due to the larger primary nozzle. Therefore, momentum builds up in the CAS

is minimal and the P_{cr} stays constant till NXP = 0 mm. Afterward, the primary shock train merges with the secondary high momentum region producing strong secondary shock wave losing the flow momentum (Figure 4.10). This eventually sharply decreases the critical back pressures as NXP is increase beyond 0 mm. It is further observed that the critical back pressure values for Ma = 4, which is a case of almost complete expansion, are smaller than for rest of the Ma number cases. Furthermore, the values of P_{cr} for Ma = 2, 3 and 5 are comparable in NXP values from −5 mm through 10 mm.

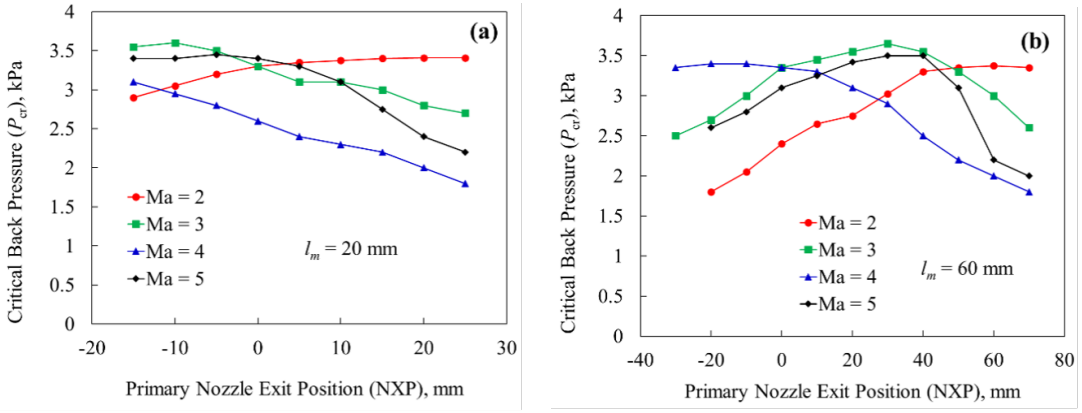

FIGURE 4.16: Line plots of the P_{cr} for all Ma number cases plotted against the NXP for (a) l_m = 20 mm and (b) l_m = 60 mm

4.2.2 l_m = 60 mm

For the case of l_m = 60 mm, the trends of critical back pressure presented in Figure 4.16a are quite different as compared to the l_m = 20 mm case when NXP is varied over a considerable range. For Ma = 2, 3 and 5, which involves over-expansion, over-expansion and under-expansion, respectively, the P_{cr} values increase as NXP is increased from −30 mm to 40 mm. Afterward, for Ma = 2, the critical back pressure becomes constant, whereas, for Ma = 3 and 5, it decreases sharply. The increasing trend in critical back pressure till NXP = 40 mm is due to the fact that for l_m = 60 mm, ejector is sufficiently bigger and the primary shock train develops in such a manner that it increases and maintains its momentum in the CAS which is supported by strength of shock wave generated in the diverging section of the ejector. However, as the NXP value is increased beyond 40 mm, the length of the shock train has reduced significantly and momentum gain in the CAS is such that

strength of the secondary shock results in momentum loss reducing the critical back pressure (Figure 4.11). The case of Ma = 4 which is an almost complete expansion, the critical back pressure stays constant initially till NXP = 10 mm, and then decreases continuously. It is interesting to note that the trends of the critical back pressure and quite identical for Ma = 3 and Ma = 5 with a minute difference in the numerical values of the parameter as the primary nozzle position is varied. Furthermore, critical back pressures are approximately the same for NXP = 40 mm and 50 mm for Ma = 2, 3 and 5.

4.3 Comparative Plots of Performance Parameters for l_m = 20 mm and l_m = 60 mm

In this section, the effects of l_m on the performance of an ejector are analyzed by comparing the results of ω and P_{cr} for l_m = 20 mm and l_m = 60 mm for each Ma number discussed in this study. Figure 4.17a presents the results of the entrainment ratio and Figure 4.17b presents the results for the P_{cr} for Ma = 2, which is the case of under-expansion. It is found that the ω decreases continuously for l_m = 20 mm and flattens out as the primary nozzle approaches and enters the CAS of the ejector. In comparison, for l_m = 60 mm, the entrainment ratio is quite low at low NXP values; first it increases and then decreases as the NXP value is increased. At NXP = 0, the entrainment ratio is almost the same for both lm values. The P_{cr}, on the other hand, increases as primary nozzle moves towards the CAS and tends to become constant as the primary nozzle approaches and enters the CAS. The P_{cr} values for l_m = 20 mm are higher as compared to l_m = 60 mm as primary nozzle is far from the CAS. However, as the primary CD nozzle approaches close to the CAS, approximately the same values are observed for the P_{cr} for both cases. The reasoning of these trends is already discussed using the contour plots in the previous section.

For Ma = 3, which is also a case of under-expansion, the results are presented in Figure 4.18. It is observed that, for l_m = 20 mm, the entrainment ratio continuously decreases as the primary CD nozzle is advanced towards the CAS. For

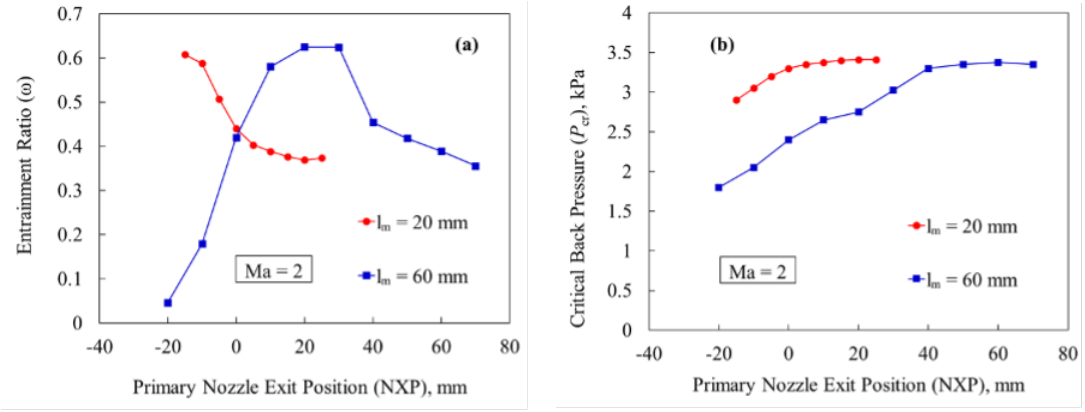

FIGURE 4.17: The performance parameters (a) Entrainment ratio and (b) Critical back pressure plotted for Ma = 2 for l_m = 20 mm and l_m = 60 mm for different values of NXP.

l_m = 60 mm, however, the ω first rises and then continuously falls as NXP value is increased. For all the values of NXP, the entrainment ratio is greater for l_m = 60 mm as compared to l_m = 20 mm. The critical back pressure for Ma = 3 presents similar values for both lm values as the NXP is varied over the defined range. For l_m = 20 mm, the P_{cr} decreases as NXP is increased. For l_m = 60 mm, P_{cr} continuously rises as the NXP is increased till NXP = 30 mm. After that, it starts decreasing due to stronger shock in the diffuser part of the ejector. At NXP = 0, for both the lm values, approximately the same critical back pressure values are reported.

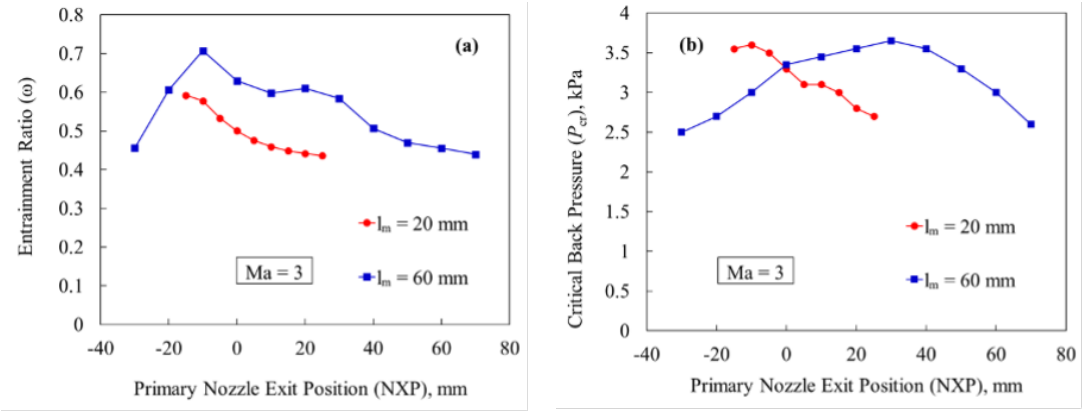

FIGURE 4.18: The performance parameters (a) Entrainment ratio and (b) Critical back pressure plotted for Ma = 3 for l_m = 20 mm and l_m = 60 mm for different values of NXP.

The trends of ω and $P_{cr}$are presented for Ma = 4 in Figure 4.19. Ma = 4 is a case of slight under-expansion. The entrainment ratio continuously decreases as the NXP value is increased. However, the behavior is quite smooth and the slope is

significantly small. The entrainment ratio values for the $l_m = 60\,\text{mm}$ are comparatively higher as compared to $l_m = 20\,\text{mm}$ at most of the corresponding instances. The critical back pressure plots presented in Section 4.3 show a continuously decreasing trend as the NXP is increased for both the values of lm. Furthermore, the P_{cr} for $l_m = 60\,\text{mm}$ is greater than that of $l_m = 20\,\text{mm}$ case at the corresponding instances.

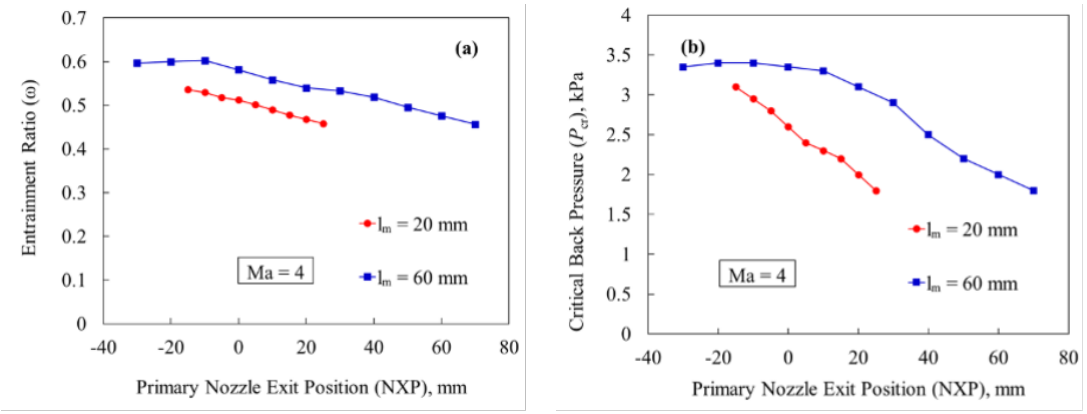

FIGURE 4.19: The performance parameters (a) Entrainment ratio and (b) Critical back pressure plotted for Ma = 4 for $l_m = 20\,\text{mm}$ and $l_m = 60\,\text{mm}$ for different values of NXP.

The trends of the performance parameters are presented for Ma = 5, which is a unique case of over-expansion, in Figure 4.20. The entrainment ratio values for $l_m = 20\,\text{mm}$ stay approximately constant as the NXP is varied until the primary nozzle exit is about to enter the constant area section of the ejector. For that case, entrainment ratio is suddenly decreased and continues to decrease as the primary nozzle moves inside the CAS. In the case of $l_m = 60\,\text{mm}$ case, the entrainment ratio shows repeated increasing and decreasing trends. When the exit of the primary CD nozzle is in the mixing chamber of the ejector's secondary nozzle, the ω for $l_m = 60\,\text{mm}$ is greater than that for the $l_m = 20\,\text{mm}$. The critical back pressure trends are presented in Section 4.3. For $l_m = 20\,\text{mm}$, the critical back pressure stays constant till NXP = 0 mm and then sharply decreases. For $l_m = 60\,\text{mm}$, the critical back pressure increases first till NXP = 40 mm and then sharply decreases.

It is observed that the ω and the P_{cr} values for any Ma number case become independent of the mixing chamber length when primary nozzle exit is placed at the entry of the CAS or inside the CAS. For $l_m = 20\,\text{mm}$, a lower value of NXP, i.e., NXP = - 10 mm gives the most favorable results of both performance

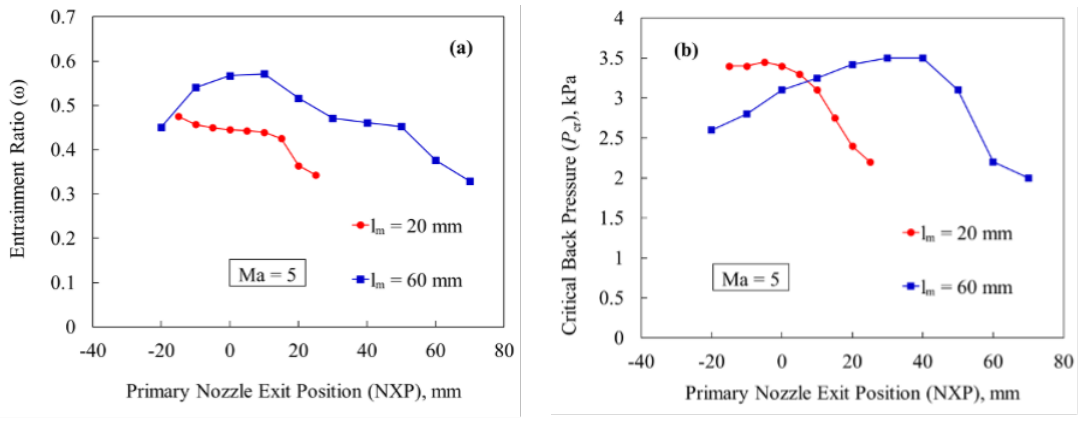

FIGURE 4.20: The performance parameters (a) ω and (b) P_{cr} plotted for Ma = 5.0 for l_m = 20 mm and l_m = 60 mm for different values of NXP.

parameters for all the Ma number cases. For l_m = 60 mm, the NXP value of 20 mm gives the most suitable combination of both performance parameters for all the Mach number cases. For NXP = - 10 mm (l_m = 20 mm) and NXP = 20 mm (l_m = 60 mm) the distances of the primary nozzle exit from the inlet of the constant area section are 30 mm and 40 mm, respectively. Therefore, 30 mm – 40 mm is a favorable range of the NXP which gives good ejector performance irrespective of the Ma and l_m.

Chapter 5

Conclusion and Future Recommendations

A computational study is performed in order to analyze effects of the geometrical variables on the performance metrics of a steam ejector applied in a refrigeration system. The present work considers an ejector geometry that is designed by Dong et al. [7]. Two geometrical variables investigated in this study are the length of the mixing chamber and the corresponding values of the NXP (position of the primary nozzle). The study is performed for the primary nozzle exit Mach numbers 2, 3, 4 and 5. The computational tool ANSYS Fluent is used to perform the simulations. A total of 80 different geometries are created, meshed, solved and analyzed. The target performance metrics considered in this investigative study are the mass entrainment ratio and the critical back pressure. Both of these parameters are to be maximized by varying the geometrical parameters. The operational parameters include the generator pressure and temperature and the evaporator pressure and temperature. All these parameters are set as per the reference study. The steam is the working fluid for which the default property database of the computation tool is used. A grid convergence study is first performed for a selected ejector geometry to decide on the suitable mesh resolution to attain grid-independent results. In order to validate the numerical solution procedure, several test cases are performed and the performance parameters are compared with the results of the reference study.

The mixing chamber lengths considered in this study are 20 mm and 60 mm. The primary nozzle positions considered for 20 mm case are: – 15 mm through 25 mm with a uniform step size of 5 mm. The primary nozzle positions for the 60 mm case are: - 30 mm through 70 mm with a uniform step size of 10 mm. The key results are as follows:

1. A series of shock waves in the shock train generated in the primary fluid jet affects the suction of secondary vapor from the evaporator. The expansion-contraction regions of the shock train dictate the available area for the entrainment of the vapor stream from the secondary inlet. These eventually dictate the performance parameter ω of the ejector.

   The momentum of primary fluid jet primarily governs P_{cr} of the ejector. The greater the momentum, the higher the P_{cr}. The higher momentum, however, produces stronger shock waves in diffuser part of the secondary nozzle if length of shock train is small, ultimately decreasing the momentum, and consequently the P_{cr}.

2. For Ma = 2, primary nozzle behaves as under-expanded nozzle producing a high Mach number outside the nozzle. The ω decreases and the P_{cr} increases as the NXP is increased by translating primary nozzle towards the constant area section for both values of l_m.

3. or Ma = 3.0, primary nozzle behaves as under-expanded nozzle as well. The ω continuously decreases when NXP is increased for both the values of l_m. The critical back pressure has a mixed increasing and decreasing trend as the NXP is increased.

4. The Ma = 4 is a case of a slight under-expansion. Both ω and P_{cr} show a progressively decreasing behavior for both values of l_m.

5. The Ma = 5 is a case of over-expansion. Therefore, again expansion and contraction regions are produced and fluctuating trends of ω are observed. The P_{cr} shows a slight increase and a sharp decrease afterward. For l_m = 20 mm, a lower value of NXP, i.e., NXP = - 10 mm gives the most favorable results of both performance parameters for all the Ma number cases. For l_m

= 60 mm, the NXP value of 20 mm gives the most suitable combination of both performance parameters for all the Mach number cases. For NXP = -10 mm (l_m = 20 mm) and NXP = 20 mm (l_m = 60 mm) the distances of the primary nozzle exit from the inlet of the constant area section are 30 mm and 40 mm, respectively. Therefore, 30 mm – 40 mm is a favorable range of the NXP which gives good ejector performance irrespective of the Ma and l_m.

5.1 Future Recommendations

There are a number of operational as well as geometrical variables that affect performance indicators of steam ejector. This makes it quite a complex optimization problem. It is recommended to use optimization techniques and machine learning algorithms to predict the performance of ejectors using available literature data.

Bibliography

[1] Hong Zhao, Ming Li, Yunfeng Wang, Ying Zhang, and Guoliang Li. Research on the characteristics of photovoltaic-driven refrigerated warehouse with ice storage in field under weather and load variation. *Renewable Energy*, 235: 121399, 2024. ISSN 0960-1481.

[2] Kanjanapon Chunnanond and Satha Aphornratana. Ejectors: applications in refrigeration technology. *Renewable and Sustainable Energy Reviews*, 8(2): 129–155, 2004. ISSN 1364-0321.

[3] R Yapıcı and HK Ersoy. Performance characteristics of the ejector refrigeration system based on the constant area ejector flow model. *Energy conversion and management*, 46(18-19):3117–3135, 2005.

[4] Nehad Al-Khalidy. An experimental study of an ejector cycle refrigeration machine operating on r113: Etude expérimentale d'une machine frigorifique à éjecteur au r113. *International journal of refrigeration*, 21(8):617–625, 1998.

[5] Gianfranco Angelino and Costante Invernizzi. Thermodynamic optimization of ejector actuated refrigerating cycles. *International journal of refrigeration*, 31(3):453–463, 2008.

[6] Kazuyasu Matsuo, Yoshiaki Miyazato, and Heuy-Dong Kim. Shock train and pseudo-shock phenomena in internal gas flows. *Progress in aerospace sciences*, 35(1):33–100, 1999.

[7] Jingming Dong, Qiuyu Hu, Mengqi Yu, Zhitao Han, Wenbin Cui, Daliong Liang, Hongbin Ma, and Xinxiang Pan. Numerical investigation on the influence of mixing chamber length on steam ejector performance. *Applied Thermal Engineering*, 174:115204, 2020.

[8] Giorgio Besagni, Riccardo Mereu, and Fabio Inzoli. Ejector refrigeration: A comprehensive review. *Renewable and Sustainable Energy Reviews*, 53:373–407, 2016.

[9] Bourhan M. Tashtoush, Moh'd A. Al-Nimr, and Mohammad A. Khasawneh. A comprehensive review of ejector design, performance, and applications. *Applied Energy*, 240:138–172, 2019. ISSN 0306-2619.

[10] K. Pianthong, W. Seehanam, M. Behnia, T. Sriveerakul, and S. Aphornratana. Investigation and improvement of ejector refrigeration system using computational fluid dynamics technique. *Energy Conversion and Management*, 48(9):2556–2564, 2007. ISSN 0196-8904.

[11] Haowei Guo, Lei Wang, and Xinli Wang. A full operating conditions ejector model for refrigeration systems driven by low-grade heat sources. *Case Studies in Thermal Engineering*, 60:104670, 2024. ISSN 2214-157X. doi: https://doi.org/10.1016/j.csite.2024.104670. URL https://www.sciencedirect.com/science/article/pii/S2214157X24007019.

[12] Bassil M. Anan, Mahmoud A. Kassem, and Ahmed Hamed. Comparison and performance analysis of single and double-stage in-series ejector refrigeration systems using various refrigerants. *Energy Conversion and Management*, 313:118606, 2024. ISSN 0196-8904. doi: https://doi.org/10.1016/j.enconman.2024.118606. URL https://www.sciencedirect.com/science/article/pii/S0196890424005478.

[13] Seyedeh Zeinab Sajjadi, Bijan Farhanieh, and Hossein Afshin. A high performance solar-assisted ejector expansion refrigeration cycle for residential air conditioning. *Applied Thermal Engineering*, 254:123872, 2024. ISSN 1359-4311. doi: https://doi.org/10.1016/j.applthermaleng.2024.123872. URL https://www.sciencedirect.com/science/article/pii/S1359431124015400.

[14] Hamid Hawi Ogaili, Shahram Khalilarya, Ata Chitsaz, and Parisa Mojaver. Energy, exergy, and economic performance analysis of integrated

parabolic trough collector with organic rankine cycle and ejector refrigeration cycle. *Energy Conversion and Management: X*, 25:100843, 2025. ISSN 2590-1745. doi: https://doi.org/10.1016/j.ecmx.2024.100843. URL https://www.sciencedirect.com/science/article/pii/S2590174524003210.

[15] Satha Aphornratana and Ian W Eames. A small capacity steam-ejector refrigerator: experimental investigation of a system using ejector with movable primary nozzle. *International journal of refrigeration*, 20(5):352–358, 1997.

[16] Szabolcs Varga, Armando C Oliveira, and Bogdan Diaconu. Influence of geometrical factors on steam ejector performance–a numerical assessment. *International journal of refrigeration*, 32(7):1694–1701, 2009.

[17] Xiaoli Ma, Wei Zhang, S.A. Omer, and S.B. Riffat. Experimental investigation of a novel steam ejector refrigerator suitable for solar energy applications. *Applied Thermal Engineering*, 30(11):1320–1325, 2010. ISSN 1359-4311.

[18] Natthawut Ruangtrakoon, Satha Aphornratana, and Thanarath Sriveerakul. Experimental studies of a steam jet refrigeration cycle: Effect of the primary nozzle geometries to system performance. *Experimental Thermal and Fluid Science*, 35(4):676–683, 2011. ISSN 0894-1777.

[19] Natthawut Ruangtrakoon, Tongchana Thongtip, Satha Aphornratana, and Thanarath Sriveerakul. Cfd simulation on the effect of primary nozzle geometries for a steam ejector in refrigeration cycle. *International Journal of Thermal Sciences*, 63:133–145, 2013. ISSN 1290-0729.

[20] Paulo R. Pereira, Szabolcs Varga, João Soares, Armando C. Oliveira, António M. Lopes, Fernando G. de Almeida, and João F. Carneiro. Experimental results with a variable geometry ejector using r600a as working fluid. *International Journal of Refrigeration*, 46:77–85, 2014. ISSN 0140-7007.

[21] Shaojie Chen, Guangming Chen, and Lingyun Fang. An experimental study and 1-d analysis of an ejector with a movable primary nozzle that operates with r236fa. *International Journal of Refrigeration*, 60:19–25, 2015. ISSN 0140-7007.

[22] Jia Yan, Chen Lin, Wenjian Cai, Haoran Chen, and Hao Wang. Experimental study on key geometric parameters of an r134a ejector cooling system. *International Journal of Refrigeration*, 67:102–108, 2016. ISSN 0140-7007.

[23] Weina Fu, Yanxia Li, Zhongliang Liu, Hongqiang Wu, and Tongran Wu. Numerical study for the influences of primary nozzle on steam ejector performance. *Applied Thermal Engineering*, 106:1148–1156, 2016. ISSN 1359-4311.

[24] Kun Zhang, Xiaojing Zhu, Xiaotong Ren, Qinggang Qiu, and Shengqiang Shen. Numerical investigation on the effect of nozzle position for design of high performance ejector. *Applied Thermal Engineering*, 126:594–601, 2017. ISSN 1359-4311.

[25] Tongchana Thongtip and Satha Aphornratana. An experimental analysis of the impact of primary nozzle geometries on the ejector performance used in r141b ejector refrigerator. *Applied Thermal Engineering*, 110:89–101, 2017. ISSN 1359-4311.

[26] A.S. Ramesh and S. Joseph Sekhar. Experimental and numerical investigations on the effect of suction chamber angle and nozzle exit position of a steam-jet ejector. *Energy*, 164:1097–1113, 2018. ISSN 0360-5442.

[27] Jia Yan, Shengyu Li, and Zhan Liu. Numerical investigation on optimization of ejector primary nozzle geometries with fixed/varied nozzle exit position. *Applied Thermal Engineering*, 175:115426, 2020. ISSN 1359-4311.

[28] Tongchana Thongtip and Satha Aphornratana. Impact of primary nozzle area ratio on the performance of ejector refrigeration system. *Applied Thermal Engineering*, 188:116523, 2021. ISSN 1359-4311.

[29] Vu Van Nguyen, Szabolcs Varga, Joao Soares, Vaclav Dvorak, and Armando C. Oliveira. Applying a variable geometry ejector in a solar ejector refrigeration system. *International Journal of Refrigeration*, 113:187–195, 2020. ISSN 0140-7007.

[30] José Galindo, Vicente Dolz, Andrés Tiseira, and Alberto Ponce-Mora. Numerical assessment of the dynamic behavior of a solar-driven jet-ejector refrigeration system equipped with an adjustable jet-ejector. *International Journal of Refrigeration*, 121:168–182, 2021. ISSN 0140-7007.

[31] Karim Abbady, Nawaf Al-Mutawa, and Abdulrahman Almutairi. The performance analysis of a variable geometry ejector utilizing cfd and artificial neural network. *Energy Conversion and Management*, 291:117318, 2023. ISSN 0196-8904.

[32] Dongjun Guo, Jianbo Wang, and Zhisong Zhu. Numerical investigation on performance optimization of steam ejector considering full geometric parameters and working conditions. *Case Studies in Thermal Engineering*, 59:104552, 2024. ISSN 2214-157X.

[33] Rafal Fingas, Michal Haida, Jacek Smolka, Lorenzo Croci, Jakub Bodys, Michal Palacz, and Giorgio Besagni. Experimental analysis of the r290 variable geometry ejector with a spindle. *Applied Thermal Engineering*, 258: 124632, 2025. ISSN 1359-4311.

[34] Y. Bartosiewicz, Zine Aidoun, P. Desevaux, and Yves Mercadier. Numerical and experimental investigations on supersonic ejectors. *International Journal of Heat and Fluid Flow*, 26(1):56–70, 2005. ISSN 0142-727X.

[35] Y. Bartosiewicz, Z. Aidoun, and Y. Mercadier. Numerical assessment of ejector operation for refrigeration applications based on cfd. *Applied Thermal Engineering*, 26(5):604–612, 2006. ISSN 1359-4311.

[36] T. Sriveerakul, S. Aphornratana, and K. Chunnanond. Performance prediction of steam ejector using computational fluid dynamics: Part 1. validation of the cfd results. *International Journal of Thermal Sciences*, 46(8):812–822, 2007. ISSN 1290-0729.

[37] T. Sriveerakul, S. Aphornratana, and K. Chunnanond. Performance prediction of steam ejector using computational fluid dynamics: Part 2. flow

structure of a steam ejector influenced by operating pressures and geometries. *International Journal of Thermal Sciences*, 46(8):823–833, 2007. ISSN 1290-0729.